minerals

MDPI

Article

The Effect of Wetting–Drying Cycles on the Deterioration of the Physical and Mechanical Properties of Cemented Paste Backfill in Open-Pit Coal Mines

Tao Chen [1,2,3], Jisen Shu [1,2,3,*], Liu Han [1,2], Zhaowan Tan [3] and Jinxing Lyu [1,4]

[1] School of Mines, China University of Mining and Technology, Xuzhou 221116, China; chentao2020@cumt.edu.cn (T.C.); hanliucumt@163.com (L.H.); lvjinxing@xju.edu.cn (J.L.)
[2] Key Laboratory of Coal Resources and Safe Mining, Xuzhou 221116, China
[3] Yunnan·Top Field-Mining Sci & Tech., Ltd., Kunming 650200, China; 13908761211@139.com
[4] School of Geology and Mines, Xinjiang University, Urumqi 830047, China
* Correspondence: jsshu888@cumt.edu.cn

Abstract: To promote the sustainable exploitation of open-pit coal resources, waste is used as backfill material to realize the comprehensive utilization of solid waste mine resources. We proposed a mining method that is a combination of the highwall mining and filling mining methods. Cemented paste backfill (CPB) samples were prepared with high-clay-mineral-content marl particles as aggregate and normal Portland cement, sulfoaluminate cement and gypsum as cementing materials. The physical and mechanical properties and microstructural evolution of CPB with different binder ratios under wetting–drying cycles were measured. The results showed that the CPB with 0–3 wetting–drying cycles underwent shear and tensile coalescence, and that with 4–10 cycles underwent shear coalescence. The unconfined compressive strength (UCS) and elastic modulus (EM) decreased exponentially with increasing number of wetting–drying cycles but decreased exponentially and cubically with increasing porosity, respectively. The EM is more sensitive to gypsum content than the UCS. CPB deterioration was divided into an initial deterioration stage and a secondary deterioration stage. The evolution curve of the total damage variable presents an 'S' shape, with an initial damage stage, an accelerated damage expansion stage, a decelerated damage expansion stage and an end damage stage. The research results provide a basis for improving the recovery rate of resources under highwall conditions, and the extensive utilization of stripping materials, and promote the coordinated development of coal resource exploitation and environmental protection.

Keywords: highwall filling mining; cemented paste backfill; wetting–drying cycle; bond strength; damage evolution

Citation: Chen, T.; Shu, J.; Han, L.; Tan, Z.; Lyu, J. The Effect of Wetting–Drying Cycles on the Deterioration of the Physical and Mechanical Properties of Cemented Paste Backfill in Open-Pit Coal Mines. *Minerals* **2024**, *14*, 296. https://doi.org/10.3390/min14030296

Academic Editors: Kun Du, Jianping Sun and Abbas Taheri

Received: 25 November 2023
Revised: 23 February 2024
Accepted: 27 February 2024
Published: 11 March 2024

1. Introduction

In recent years, the proportion of open-pit mining in the world's mining industry has been increasing, resulting in a large amount of waste and causing a series of environmental problems, such as the spontaneous combustion of coal gangue [1], release of excessive soil heavy metals [2], ecological damage [3], acid mine drainage (AMD) [4], collapse of mining areas [5] and other issues. Over the past decades, many scientists from the United States, Canada, Australia and other countries have been working on coal waste management and environmental issues in depth [6]. For example, the establishment of coal-based solid waste dams and coal slurry impoundments [7], coal-based solid waste as construction materials (cement [8], road base materials [9], asphalt [10], environmental brick [11], coal waste-derived soil-like substrate [12], microbiological liquefaction of lignite and mechanochemical oxidative modification for the treatment of solid waste resources [13,14], backfilled roadways [15], AMD industrial extraction of metal elements [16] and dewatering for landfill [17], etc.

After high-intensity mining, open-pit coal mines leave a considerable amount of coal resources within the mining boundary. Due to the previous lack of coal mining theory and poor mining technologies, coal resources have been wasted [18]. At this time, waste is backfilled to the stope and adit, which not only improves the recovery rate of coal resources but also realizes the comprehensive utilization of solid waste mine resources as CPB [19]. However, in the process of coal mining, in the complex geological environment, rainfall easily infiltrates into the interior of the mining chamber along fault fracture zones and slope steps [20]. At the same time, groundwater easily infiltrates the adit along fractures after coal mining [21]. The exposure of CPB to air and water cause it to repeatedly undergo wetting–drying cycles [22], so the CPB is degraded by the water–rock chemical reaction [23], as shown in Figure 1. Therefore, it is necessary to study the solid waste utilization method of open-pit coal mines and CPB performance under wetting–drying cycles.

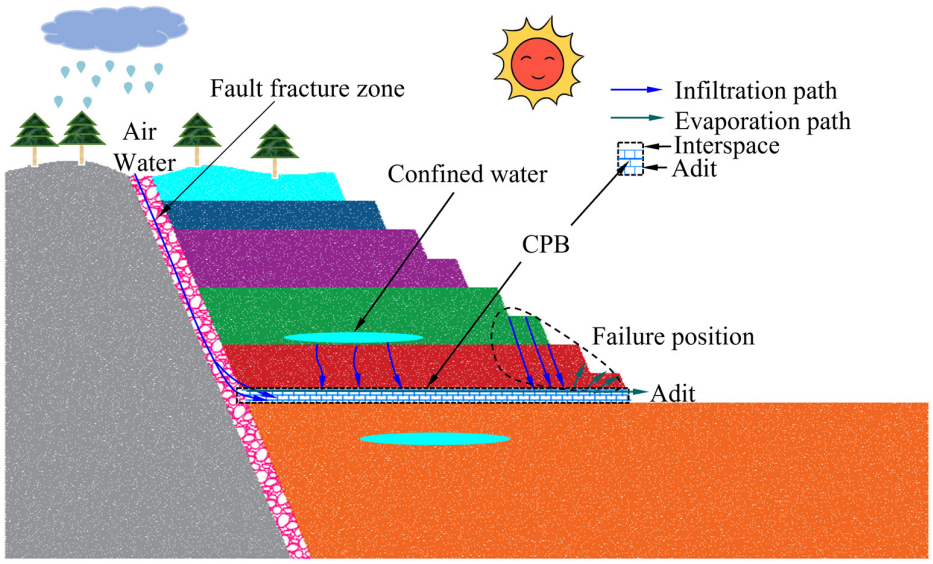

Figure 1. Wetting–drying cycle diagram of CPB under an open-pit coal mine slope.

Most of the striped rock layers in open-pit coal mines belong to geological soft rock, often containing a large amount of expansive clay minerals, which easily soften, expand and disintegrate in water [24]. Currently, with CPB with waste as the aggregate, clay minerals and their influence on its performance need to be considered [25]. Previous studies on backfill materials containing clay minerals under wetting–drying cycles mainly focused on the effect of gypsum on backfill. Aldaood et al. [26] showed that, under wetting–drying cycles, the higher the gypsum content, the greater the crack propagation and the smaller the unconfined compressive strength (UCS) of the soil sample. Durgun [27] found that polypropylene reduces the negative effects of wetting–drying cycles on gypsum-containing basalt pumice, reducing the loss of flexural strength to less than 7%. Li et al. [28] believed that extending the curing period of gypsum-treated soil samples from 7 days to 21 days could reduce the formation of vertical cracks during soaking. Ying et al. [29] indicated that wetting–drying cycles softened gypsum-treated soil and that seawater was more likely to cause macropore development than deionized distilled water. Although these studies have increased the understanding of the effect of wetting–drying cycles on gypsum-treated soil, there has been no relevant experimental study on the effect of CPB containing clay minerals, and the degree and mechanism of deterioration need further study.

Studies have shown that wetting–drying cycles have a significant effect on the water physical and mechanical properties of rocks [30]. With the increase in the number of wetting–drying cycles, the water absorption and porosity of rock [31,32], the crack propagation radius decreases [33], and the mechanical properties, such as UCS, EM, cohesion and internal friction angle, gradually decrease [34,35]. The dissolution and loss of soluble minerals and increased permeability are the key factors for the deterioration effect of a

wetting–drying cycle [36]. However, for soft rock with a high clay mineral content, the expansion/contraction behavior of clay mineral particles is more serious [37,38]. Although CPB and rock have some similar characteristics, because CPB is a prefabricated material, its particle size composition and cementing material composition are very different from rock. Therefore, clay minerals and cementing materials are important to study to understand the effect of wetting–drying cycles on CPB with waste as an aggregate. At present, the mechanism of the physical and mechanical properties of CPB under this condition is not clear, and the test method can be further explored.

Many scholars have studied CPB damage evolution. Aldhafeeri and Fall [39] examined the relationship between sulfide-containing CPB reactivity and mechanical damage. Fu et al. [40] established a damage evolution model of CPB with a layered structure and introduced the concepts of initial damage, load damage and total damage. Wang et al. [41] and Zhou et al. [42] established a damage model based on the acoustic emission ringing count rate and studied the variation in damage variables and the fractal dimension during CPB damage. Yin et al. [43] proposed a CPB segmented damage constitutive model considering fiber content. Zhang et al. [44] established a CPB damage model considering initial pore damage. The above studies focused on only mechanical damage and did not involve wetting–drying cycle damage. Therefore, it is necessary to consider the establishment of a CPB damage model under wetting–drying cycles.

In view of the existing technical defects and knowledge shortcomings, we propose a method of solid waste utilization in open-pit coal mines. The water absorption crack development, dynamic evolution law of porosity, mechanical property and failure characteristics, damage evolution law and scanning electron microscopy (SEM) structure deterioration analysis of CPB with marl as aggregate under wetting–drying cycles are studied. The purpose of this work is to improve the recovery efficiency of coal resources, realize solid waste utilization, clarify the deterioration effect and damage degree of the wetting–drying cycle on CPB and promote the coordinated development of coal resource exploitation and environmental protection.

2. Materials and Methods

2.1. CPB Preparation Process

While mining coal resources in open-pit coal mines, a large amount of waste is produced, mainly the soil–rock mixture of the stripped coal seam roof and overlying strata. Therefore, this study was conducted in the context of CPB filling mining in the Puyang open-pit coal mine, China. The coal mine uses marl as the raw material of the CPB aggregate. Through grading screening, marl is broken and divided into five particle size ranging from 0–0.3 mm, 0.3–0.6 mm, 0.6–1.18 mm, 1.18–2.36 mm and 2.36–4.75 mm, as shown. To ensure the uniformity of the prepared CPB sample, Talbot continuous grading theory was used to remix the aggregate particles to meet the following relationships [45]:

$$\frac{M\left(r < \overline{d}_i\right)}{M_0} = \left(\frac{\overline{d}_i}{d_{\max}}\right)^{3-\mathrm{FD}} \tag{1}$$

where $M\left(r < \overline{d}_i\right)$ refers to the cumulative mass of rock and soil particle sizes greater than d_i; M_0 is the total mass of rock and soil particle sizes; $\overline{d} = \frac{d_i + d_{i+1}}{2} (d_i > d_{i+1}, i = 1, 2, \ldots)$ is the average value between the two particle sizes; $d_{\max}$ is the maximum rock particle size; and FD is the fractal dimension.

Three groups (No. 1–3) of particle size screening tests were carried out on marl particles of 100.00 g each. The mass of marl particles in each particle size range was calculated using Equation (1) (see Table A1). No. 4 is the average of Nos. 1–3, and the aggregate is configured with the particle mass in No. 4. Marl is a transitional rock between carbonate rock and clay rock, and its mineral composition is very important for the analysis of the CPB deterioration mechanism in subsequent wetting–drying cycles. Therefore, a

X'Pert Pro MPD (see Table A2 for detailed parameters) was used to analyze the whole rock and clay composition of the marl powder, as shown in Figure 2.

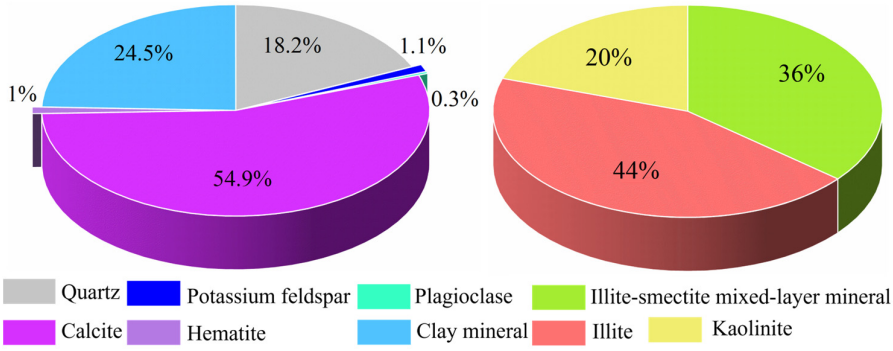

Figure 2. Mineral composition of marl minerals and clay minerals.

In this study, normal Portland cement, sulfoaluminate cement and gypsum were selected as cementing materials for the marl particles. Their basic physical properties and main component contents are shown in Tables A3–A6. Since CPB has difficulty in meeting the requirements of early strength with Portland cement alone, other reagents are often added [46]. Therefore, four different composite cementing materials were set up, and the mass ratios of normal Portland cement:sulfoaluminate cement:gypsum were 10:0:0, 8:0:2, 8:1:1, and 8:2:0. At room temperature, standard samples (50 mm in diameter and 100 mm in height) were prepared by cementing material and marl aggregate with a cement–sand ratio of 1:4.23 and a slurry concentration of 76%. A sample was placed at a temperature of 20 ± 5 °C for 24 h until solidified; then, it was numbered, demolded and placed in a SHBY-40A cement standard curing box with a temperature of 22 °C and a humidity of 95% for 28 days. The sample preparation process is shown in Figure 3.

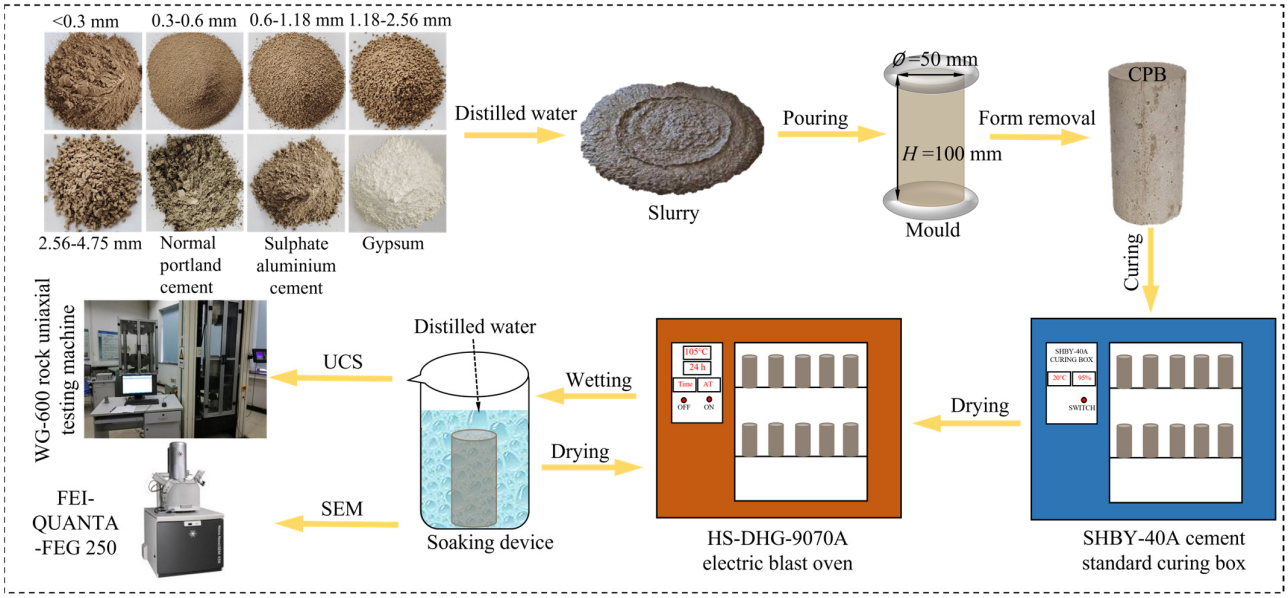

Figure 3. CPB sample preparation and wetting–drying cycle test process.

2.2. Experimental Process

2.2.1. Wetting–Drying Cycle Test

To study the effect of wetting–drying cycles on the water physical and mechanical properties of CPB, 48 samples were divided into 8 groups in the experimental design scheme. A wetting–drying cycle determination test, wetting–drying cycle test and UCS test were carried out, in that order. The specific scheme of each test is shown in Table 1. Before

the wetting–drying cycle test, all CPB samples that had been cured for 28 days were placed in an electric blast oven at 105 °C (see Table A7 for detailed parameters) for a 24 h drying treatment and then sealed with a preservative film.

Table 1. Experimental scheme design.

Sample Number	Test Classification	Normal Portland Cement:Sulphoaluminate Cement:Gypsum	Wetting–Drying Cycles	Number of Samples
WD-1~3	Wetting–drying cycle time determination test	8:1:1	1	3
RU1~4	Wetting–drying cycle test	10:0:0	10	1
RU2~4		8:0:2	10	1
RU3~4		8:2:0	10	1
RU1-1~3	Wetting–drying cycle test; UCS test	10:0:0	5	3
RU2-1~4		8:0:2	5	3
RU3-1~4		8:2:0	5	3
RU4-0~10-1~3		8:1:1	0~10	33

To determine the wetting–drying cycle time, a preliminary test was performed using the method of Ma et al. [22] to obtain the time it took the CPB to reach saturation and then fully dry. The dry CPB samples without wetting–drying cycles were designated as experiencing 0 cycles. First, three initial CPB samples (WD-1~3) were immersed in deionized distilled water with a pH value of 7 at room temperature by the free immersion method and then dried in an electric blast oven at 105 °C. The CPB samples were weighed every 5 min during immersion and every 1 h during drying. When the mass of the CPB sample remained unchanged, it was considered that the CPB sample had reached a saturated or dry state, and the curve of the water content of the CPB sample with time is shown in Appendix C. According to the wetting–drying cycle time to determine the test results, the control standard times were determined: 105 °C drying for 10 h and room temperature soaking for 45 min. A CPB sample was immersed in water at room temperature for 45 min for a wetting cycle; the sample was then dried in an oven at 105 °C for 10 h and then cooled to room temperature, to complete a wetting–drying cycle. The CPB samples were subjected to 10 wetting–drying cycles, and then immediately sealed with an impervious film.

2.2.2. UCS Test

According to the sample number in Table 1, the UCS test of the WG-600 rock uniaxial testing machine was carried out on CPB samples of different composite cementing materials under wetting–drying cycles, as shown in Figure 3. The samples were numbered RU1-1~3, RU1-2~3, RU3-1~3 and RU4-0~10-1~3 in the first wetting–drying cycle test and subsequent UCS test. Before testing, the CPB samples were processed to ensure that the deviation of the parallelism of the two ends was not greater than 0.1 mm and that the diameter deviation was not greater than 0.2 mm. Three samples from each group were tested and loaded at a displacement rate of 0.50 mm/s until failure. According to the test data, a smooth stress–strain curve was drawn, and the USC and strain were obtained. The slope was solved in the relatively straight area of the curve to obtain the EM.

2.2.3. SEM Test

The water absorption, compactness and bond strength of CPB samples are determined by the distribution of microcracks, pores and hydration products with different contents of composite cementing materials under wetting–drying cycles. The microstructure of CPB samples was scanned by an FEI-QUANTA-FEG 250 scanning electron microscope under different resolution conditions, and the corresponding parameters are shown in Table A8.

2.3. Methodology

2.3.1. Highwall Filling Mining Method

Highwall mining originated in the United States and subsequently became an important means of mining open-pit coal in the United States, Australia, Indonesia and other countries [47–49]. Due to the large number of coal pillars set up in the highwall mining process [50,51], the recovery rate of highwall coal resources has not been considerably improved. Currently, nonpillar mining technology by using waste as the filling aggregate has great advantages. In this study, the highwall filling mining method (Figure 4a) is proposed for the first time. It is based on the technology of mining the overlying coal seam under the highwall of the continuous shearer [52]. The filling process system is integrated, and the waste is used as the aggregate to form CPB, which completes the filling of the adit formed by the continuous shearer mining, thereby controlling the movement of the slope rock layer. The main process is as follows: the continuous shearer mining forms a series of adits in the overlying coal seam under the highwall by means of sequential skip mining, and then the wastes (coal gangue, soil–rock mixture, etc.) produced by the stripping of the working side are transported to the crushing station through the mining truck, and the wastes are broken into aggregate particles of appropriate particle size and then transported to the batching station through the belt conveyor to mix with cement materials and water to form CPB slurry. The filling pump station transports the CPB slurry to the adit through the pipeline for filling and then recovers and fills the coal pillar after the filling of the adit is completed. The specific implementation method is described in a patent [53]. Finally, the stripping–mining–transportation–filling/dumping–reclamation integrated collaborative operation is realized, as shown in Figure 4b. Through technological and conceptual innovation, green mining with zero ecological damage is achieved, which improves the recovery rate of coal resources, realizes solid waste utilization and greatly reduces the damage to the ecological environment. This mining technology was first applied to the Puyang open-pit coal mine in China.

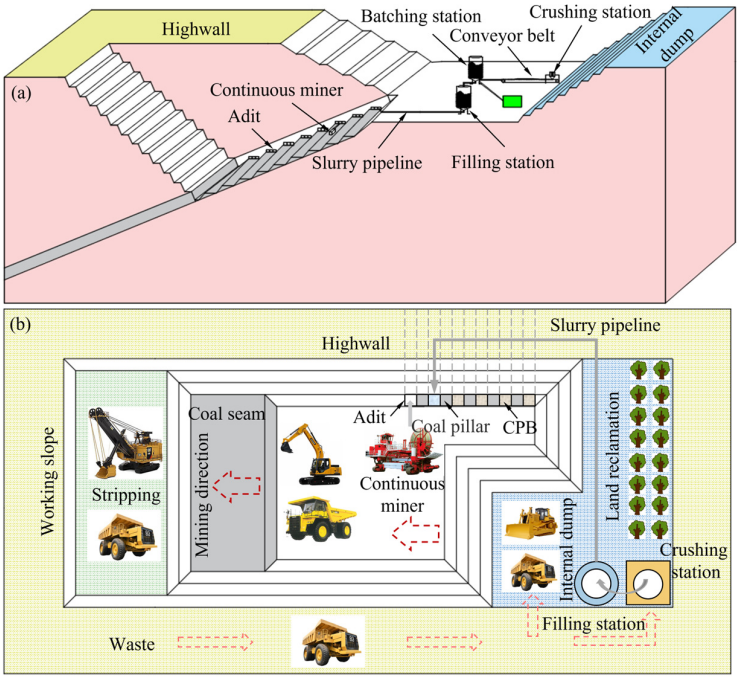

Figure 4. Schematic diagram of highwall backfill mining (**a**,**b**).

2.3.2. Porosity Calculation

Porosity is an important index with which to measure CPB and reflects the density of the CPB [54]. By testing the mass and size of the CPB during the wetting–drying cycles, the porosity φ_t of the t wetting–drying cycle can be calculated using Equation (2):

$$\varphi_t = \frac{4(m_{wt} - m_{dt})}{\pi \phi^2 H \rho_w} \tag{2}$$

where m_{wt} is the mass of the CPB sample after water absorption (g); m_{dt} is the mass of the CPB sample after drying (g); ϕ is the diameter of the CPB sample (cm); H is the height of the CPB sample (cm); and ρ_w is the density of deionized distilled water (g/cm^3), which is 1 g/cm^3.

2.3.3. Deterioration Degree of CPB

Previous studies have shown that wetting–drying cycles have different degrees of influence on CPB. To further analyze the influence of the number of wetting–drying cycles on the deterioration of the UCS and EM of CPB samples, Equations (3) and (4) were used to calculate the following:

$$D_\sigma = \frac{\sigma_t - \sigma_{t+1}}{\sigma_t} \times 100\% \tag{3}$$

$$D_E = \frac{E_t - E_{t+1}}{E_t} \times 100\% \tag{4}$$

where D_σ and D_E are the deterioration degrees of UCS and EM, respectively; σ_t and E_t are the UCS (MPa) and EM (GPa) of wetting–drying cycle t; and σ_{t+1} and E_{t+1} are the UCS (MPa) and EM (GPa) of wetting–drying cycle $t + 1$.

2.3.4. Damage Model of CPB

Under the combined action of the wetting–drying cycles and load, the CPB damage variable can be expressed by the generalized damage variable D (Xu et al., 2017) obtained by the equivalent strain principle [55]:

$$D = D_w + D_L - D_w D_L \tag{5}$$

where D is the damage variable under the coupling of the wetting–drying cycle and load; D_W is the damage variable under the wetting–drying cycles; and D_L is the damage variable under load.

The change in microstructure leads to a change in the macroscopic mechanical properties. Therefore, the damage variable of the damaged part of the sample after wetting–drying cycles can be defined with the macroscopic mechanical properties EM of CPB, namely,

$$D_w = 1 - E_t / E_0 \tag{6}$$

where E_0 is the EM of CPB with 0 wetting–drying cycles.

Assuming that the CPB strength obeys a Weibull distribution, the damage variables of the CPB under the load [56] are

$$D_L = \int_0^\varepsilon Q(x)\mathrm{d}x = 1 - \exp\left[-(\varepsilon/\xi)^m\right] \tag{7}$$

where $Q(x)$ is the probability density function; ε is the strain value of CPB; and m and ξ are parameters that characterize the physical and mechanical properties of CPB, which can be determined by the peak strength σ_p on the stress–strain curve and its corresponding peak strain ε_p.

Bringing Equations (6) and (7) into Equation (5),

$$D = 1 - \frac{E_t}{E_0} \exp\left[-(\varepsilon/\xi)^m\right] \tag{8}$$

According to Hooker's theorem, in the case of one-dimensional elasticity, the basic relationship of the damage constitutive can be obtained according to the Lemaitre strain equivalence principle [57]:

$$\sigma = E_t \varepsilon (1 - D_L) \tag{9}$$

where σ is the stress of the CPB.

Taking Equation (7) into Equation (9), the CPB damage constitutive model equation under the coupling of the wetting–drying cycle and load can be obtained as follows:

$$\sigma = E_t \varepsilon \exp\left[-(\varepsilon/\xi)^m\right] \tag{10}$$

The derivative of Equation (10) is

$$\frac{\partial \sigma}{\partial \varepsilon} = E_t \left(1 + m(-\varepsilon/\xi)^m\right) \exp\left[-(\varepsilon/\xi)^m\right] \tag{11}$$

According to the geometric control equation, when $\varepsilon = \varepsilon_p$, $\sigma = \sigma_p$; when $\varepsilon = \varepsilon_p$, $\partial\sigma/\partial\varepsilon = 0$; and

$$\begin{cases} \sigma_p = E_t \varepsilon_p \exp\left[-\left(\varepsilon_p/\xi\right)^m\right] \\ E_t \left(1 - m\left(\varepsilon_p/\xi\right)^m\right) \exp\left[-\left(\varepsilon_p/\xi\right)^m\right] = 0 \end{cases} \tag{12}$$

The parameters m and ξ can be obtained from Equation (12):

$$m = \frac{1}{\ln\left(E_t \varepsilon_p / \sigma_p\right)} \tag{13}$$

$$\xi = \varepsilon_p / \left(m^{-1}\right)^{m^{-1}} \tag{14}$$

The damage evolution equation and damage constitutive model equation of CPB are obtained by bringing Equations (13) and (14) into Equations (8) and (10), respectively:

$$D = 1 - \frac{E_t}{E_0} \exp\left[-\frac{1}{m}\left(\varepsilon/\varepsilon_p\right)^m\right] \tag{15}$$

$$\sigma = E_t \varepsilon \exp\left[-\frac{1}{m}\left(\varepsilon/\varepsilon_p\right)^m\right] \tag{16}$$

2.3.5. Data Processing Statistics

This study used OriginPro2021 to visualize the data and Microsoft Excel 2019 to perform statistical analysis. The mean $\overline{X}$ (Equation (17)) and standard deviation S (Equation (18)) were used to analyze the porosity, UCS and EM of the CPB samples after each wetting–drying cycle. The calculation equations are as follows:

$$\overline{X} = \frac{1}{N} \sum_{i=1}^{N} X_i \tag{17}$$

$$S = \sqrt{\frac{\sum_{i=1}^{N} \left(X_i - \overline{X}\right)^2}{N - 1}} \tag{18}$$

where X_i refers to the porosity, UCS and EM of a CPB sample in the same group, and N refers to the number of the three CPB samples in the same group.

3. Results

3.1. Water Physical

3.1.1. Crack Propagation Law

The CPB samples with a composite cementing material ratio of 8:1:1 were subjected to 10 wetting–drying cycles. For the zero–two wetting–drying cycle CPB samples, the surface of the samples remained intact, and no visible microcracks were found, as shown in Figure 5a–c. In the process of three~four wetting–drying cycles, a few pinnate microcracks formed on the upper surface of the samples, and the range of microcracks was small, as shown in Figure 5d,e. Starting from the fifth cycle, pinnate microcracks and other microcracks appeared in the upper and middle parts of the sample surface, as shown in Figure 5f. During the sixth cycle, V-type microcracks appeared on the upper part of the sample, the crack length increased and the microcracks gradually expanded, as shown in Figure 5g. During the seventh and eighth cycles, crack microcracks and V-type microcracks were generated in the upper and middle parts of the samples, and the range of microcracks gradually expanded, as shown in Figure 5h,i. During the 9th and 10th cycles, microcracks and cracks appeared on the surface of the samples, the microcracks gradually expanded into Y-type cracks and axial cracks and the crack length and range increased, as shown in Figure 5j,k. According to the change in cracks, the crack propagation of CPB samples in the wetting–drying cycles can be divided into several stages: fine crack formation stage—V-type, pinnate microcrack development stage—crack microcrack formation stage—Y-type crack propagation stage.

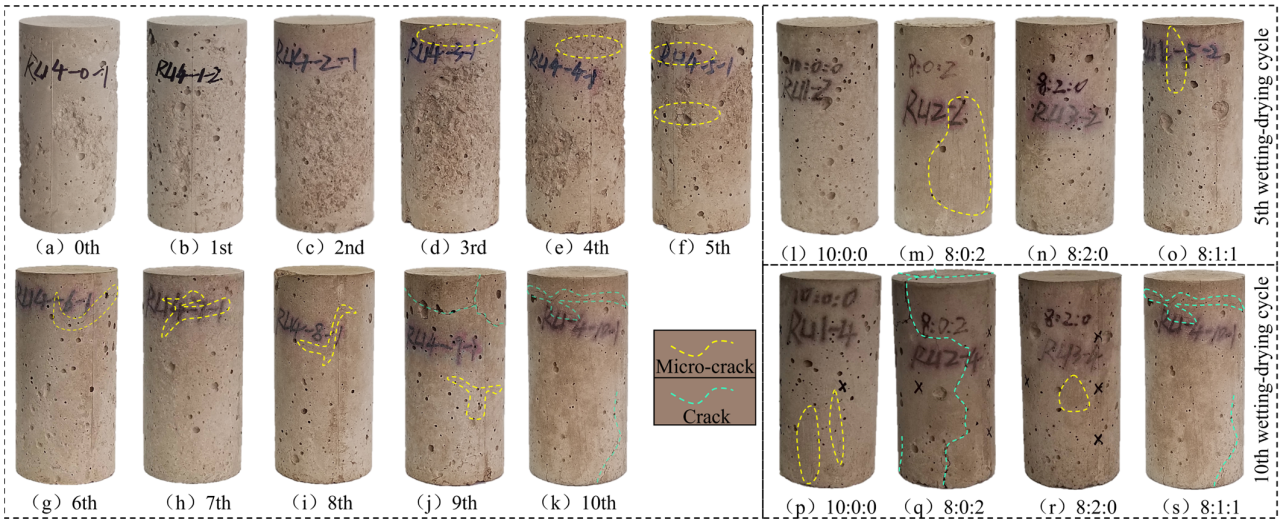

Figure 5. Effect of wetting–drying cycles on CPB surface crack propagation.

Figure 5l–s shows that the surface crack propagation trends of CPB samples with different cementation contents are significantly different. In the process of five wetting–drying cycles, samples RU1-2 and RU3-2 (which did not contain gypsum) still maintained surface integrity, and no visible microcracks were found. However, many microcracks appeared on the surface of the RU2-2 and RU4-5-2 samples. Linear cracks appeared in the middle and lower parts of sample RU2-2, and pinnate microcracks appeared in the upper part of sample RU4-5-2. In the process of 10 wetting–drying cycles, samples RU1-4 and RU3-4 with composite cementing material ratios of 10:0:0 and 8:2:0 exhibited a few visible microcracks, and the microcracks were linear. The surfaces of samples RU2-4 and RU4-10-2 with composite cementing material ratios of 8:0:2 and 8:1:1 showed many cracks, and the crack propagation and development degree of sample RU2-4 were significantly more serious than those of sample RU4-10-2. The top crack of sample RU2-4 shows a cross type, and the crack propagates across the whole surface of the sample. The upper surface of sample RU4-10-2 shows a Y-type crack, and the lower part shows a linear crack.

3.1.2. Variation in Porosity

The porosity curves of CPB samples with four different cementation ratios were obtained by a wetting–drying cycle test. The initial porosity of all samples was approximately 12.91~14.39%, as shown in Figure 6. Figure 6a shows that the porosity change processes of samples WD-1, WD-2 and WD-3 were almost the same, and the porosity rate increased rapidly in the first wetting–drying cycle test. The porosity of the three samples was basically in equilibrium after the fourth wetting–drying cycle. The porosity after the fourth wetting–drying cycle is plotted in Figure 6c. The porosity was between 25.88% and 27.65%, and the average porosity was 26.81%. From Figure 6b, the porosity change trends of samples RU1-4 and RU3-4 were basically consistent. The porosity of the samples with four different cementation contents increased with the number of wetting–drying cycles and finally reached a stable porosity [31]. Among them, the porosity change rates of samples RU1-4 and RU3-4 were basically the same, and the porosity change rate of sample RU4-10-1 was basically the same as that of sample WD-3, but the porosity change rate of sample RU2-4 was more complex than that of the other three samples. The equilibrium porosity histogram of Figure 6d shows that the porosity of the four samples followed the order of RU2-4 > RU4-10-1 > RU3-4 > RU1-4.

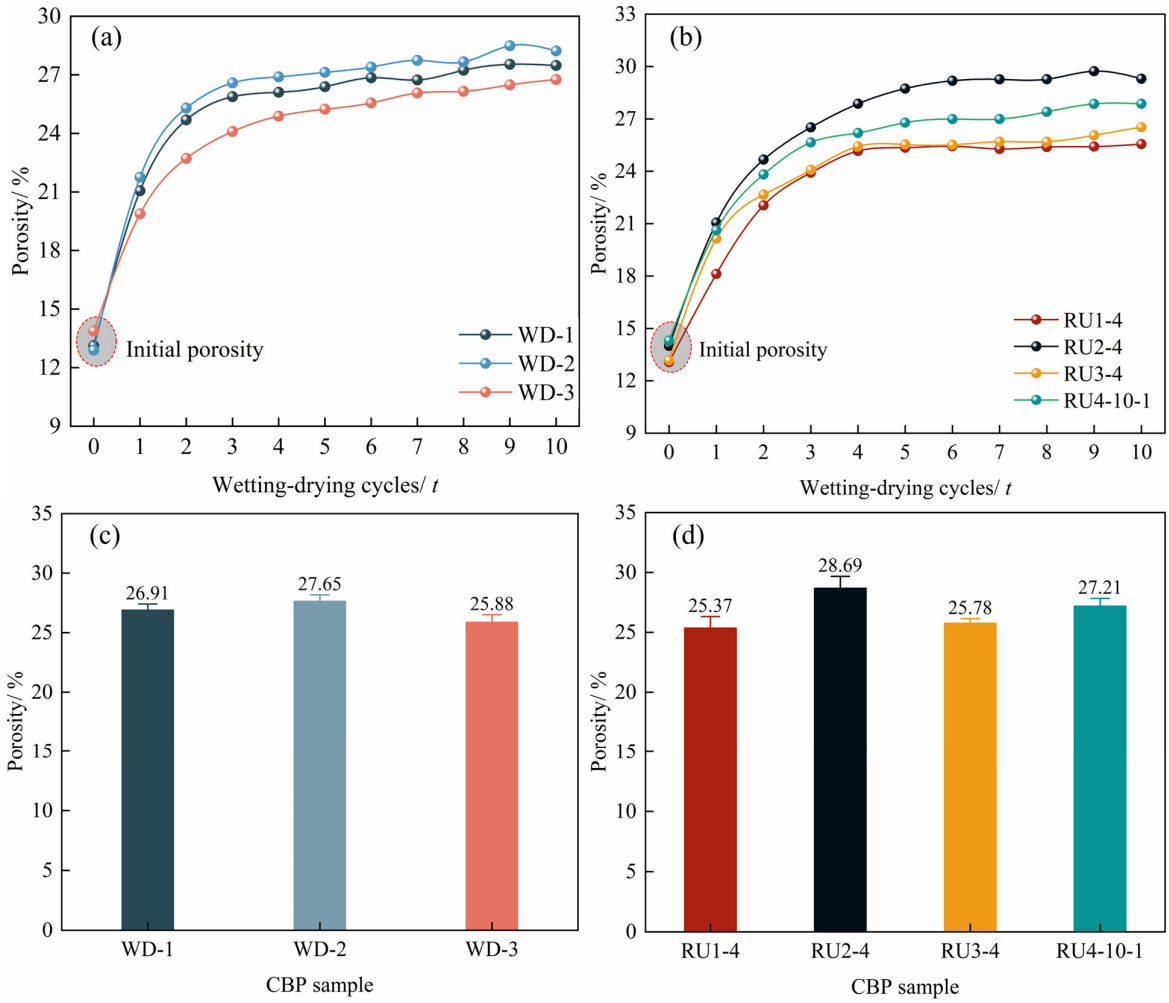

Figure 6. Changes in porosity of (**a**) samples WD-1, 2, 3 and (**b**) samples RU1, 2,3-4 and RU4-10-1 with with wetting-drying cycles; average values of porosity of (**c**) samples WD-1, 2, 3 and (**d**) samples RU1, 2,3-4 and RU4-10-1 after the fourth wetting-drying cycle.

3.2. Variation in Mechanical Properties

3.2.1. Stress–Strain Curve

Figure 7a–c shows the CPB stress–strain curve for 0–10 wetting–drying cycles. The results show that, with the increase in the number of wetting–drying cycles, the original pore compaction stage of CPB increased, the peak stress decreased and the peak strain increased. In the process of 0–10 wetting–drying cycles, the stress–strain curve shows an S-type shape; the CPB had high compressibility and plastic–elastic-plastic characteristics. With 0–3 wetting–drying cycles, the CPB cementation strength was high, the surface of the sample remained intact and the internal pores and microcracks were underdeveloped. As shown in Figure 5, the original pore compaction stage was shortened, the change rate of the stress–strain curve was fast and the peak stress changed greatly, but the peak strain was not much different. In the process of 4–10 wetting–drying cycles, the pores and voids in the sample increased, resulting in a weak CPB cementation ability, low strength, gentle stress–strain curve slope, a small change in the peak stress and a large change in the peak strain.

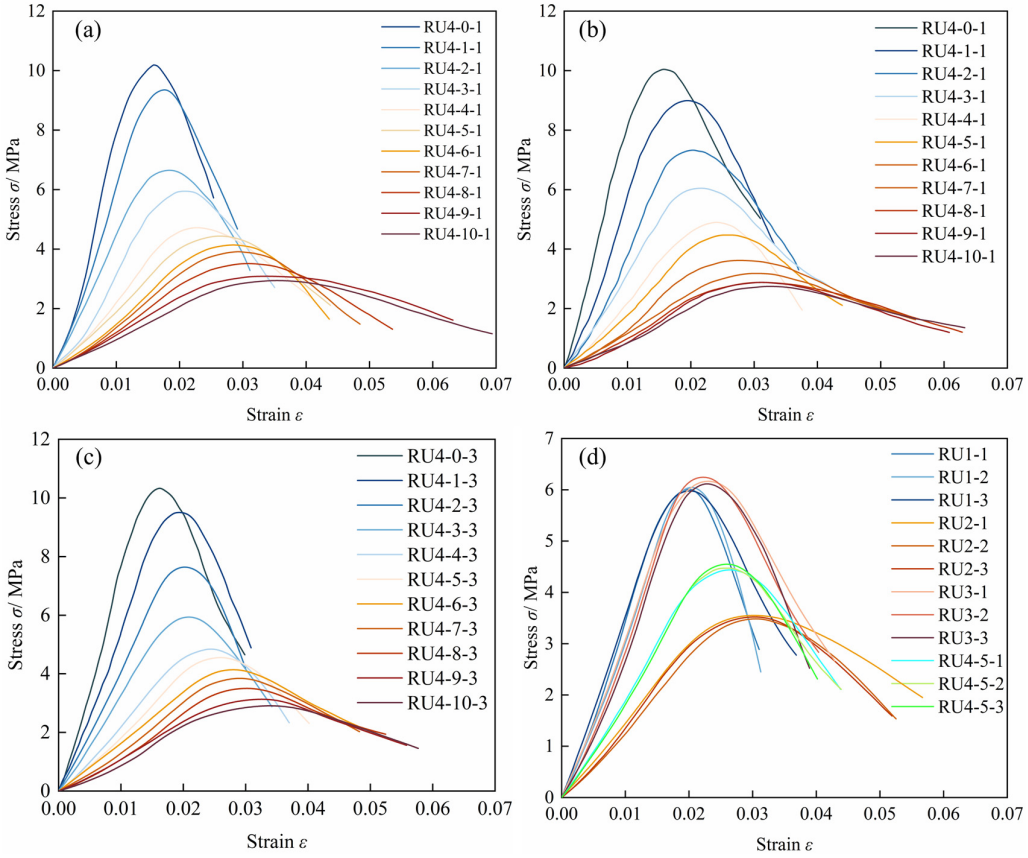

Figure 7. Stress-strain curves of (**a**) RU4-0~10-1, (**b**) RU4-0~10-2, (**c**) RU4-0~10-3, (**d**) RU1-1~3, RU2-1~3, RU3-1~3, RU4-5-1~3 under different wetting-drying cycles.

Figure 7d shows the stress–strain curves of CPB samples with different composite binders after five wetting–drying cycles. The cementation strength of samples RU1 and RU3 was significantly greater than that of samples RU2 and RU4. Among them, the peak strength of RU1 and RU3 was approximately 6.00 MPa. The strength of the CPB samples with the four different composite cementing materials followed the order of RU1 ≈ RU3 > RU4 > RU2, indicating that CPB samples with only normal Portland cement or mixed with sulphoaluminate cement have better anti-degradation performance during wetting–drying cycles. However, the cementation performance of the samples mixed with gypsum is poor. The greater the amount of incorporation, the worse the performance of the sample after the wetting–drying cycle, and the more serious the deterioration of the sample.

The peak strain of samples RU1 and RU3 was significantly smaller than that of RU2 and RU4, and RU2 > RU4, suggesting ductile failure [58]. From the original pore compaction stage, the order of the compression time was RU2 > RU4 > RU3 > RU1. RU2 > RU4 because, for sulfate cement in the early stages, the higher the heat of hydration [59], the more dry shrinkage and bubbles, so that the addition of sulfate cement to normal Portland cement increases the initial porosity. RU3 > RU1, because gypsum also forms more small bubbles in the early hardening process, and in the subsequent wetting–drying cycle, gypsum and clay minerals react with water to hydrate, resulting in an increase in pores in the sample [60].

3.2.2. Failure Mode and Characteristics

In 1960, Griggs performed a statistical analysis to classify rock uniaxial compression failure. According to the strain corresponding to the peak stress in the stress–strain curve, rock deformation can be divided into brittle failure, brittle–ductile transition failure and ductile failure [58]. Figure 7 shows that the strain value of the CPB sample to reach the peak stress is between 1.5% and 3.5%. If there is a relatively complete stress–strain curve, the CPB sample is judged to be in ductile failure. This is consistent with the results of Zhao et al. [61]. Bobet and Einstein [62] carried out uniaxial compression tests on prefractured gypsum samples and proposed a mechanism of crack coalescence under uniaxial compression: the mechanism of shear coalescence is usually characterized by a crack propagation path with twists and turns, rough crack edges, and more broken particles in the sample; the tensile penetration shows that there are no broken solid particles on the crack surface, and the crack edge is relatively smooth. Shear and tensile coalescence conforms to failure between the two. Combined with Figure 8, it was found that there are fewer main cracks in samples RU4-0, RU4-1, RU1 and RU3, and that there are fewer secondary cracks around the main cracks. The edge of a crack is relatively regular, but there is local falling debris. Therefore, it was determined that the penetration form of these CPB cracks is shear and tensile penetration. The main cracks of RU2 and RU4-2~RU4-9 are more numerous, and the crack propagation path, with more secondary cracks, is more tortuous and prone to form debris and cause debris falls, which indicates that the crack coalescence form of these samples is shear coalescence. This shows that the crack propagation of CPB is not only affected by the particle size distribution and mechanical damage but also related to the properties of the cementing materials and wetting–drying cycle damage.

The uniaxial compression failure mode of CPB with a composite cementing material ratio of 8:1:1 under 0–10 wetting–drying cycles is shown in Figure 8. The number of wetting–drying cycles had a significant effect on the damage morphology of the CPB. In the CPB that was not affected by the wetting–drying cycling, the main crack gradually expanded along the loading direction, and the two main cracks were obviously parallel to the axial stress direction, accompanied by more secondary cracks. When the compression energy reached the critical value, the local surface of the sample exhibited a spalling phenomenon and, finally, the main crack penetrated the sample instability failure, as shown in Figure 8 (RU4-0). The angle between the main crack and the axial stress direction of the sample with one wetting–drying cycle gradually increased, the secondary cracks were smaller and small debris appeared in localized places at the end, as shown in Figure 8 (RU-1). After two–four wetting–drying cycles of the sample, the main crack direction was diagonal across the sample, and the number of main cracks gradually increased. The surface of the sample exhibited a small amount of large pieces of falling debris and more broken small pieces. The end of the sample damage was more seriously damaged, and the sample exhibited obvious shear failure, as shown in Figure 8 (RU4-2~RU4-4). After five–six wetting–drying cycles of the samples, the main crack direction and the axial stress direction were approximately 45°, there were fewer secondary cracks, the lateral expansion of the samples under pressure was obvious and only a small number of debris falls occurred, since the samples exhibited significant shear failure, as shown in Figure 8 (RU4-5 and RU4-6). After seven–nine wetting–drying cycles of the sample, the main crack directions were roughly the two diagonal directions of the samples, the main crack development was

good and there were more secondary cracks and microcracks. However, after the failure of the sample, there were only small pieces of falling debris, and the sample showed obvious shear failure, as shown in Figure 8 (RU4-7~RU4-9).

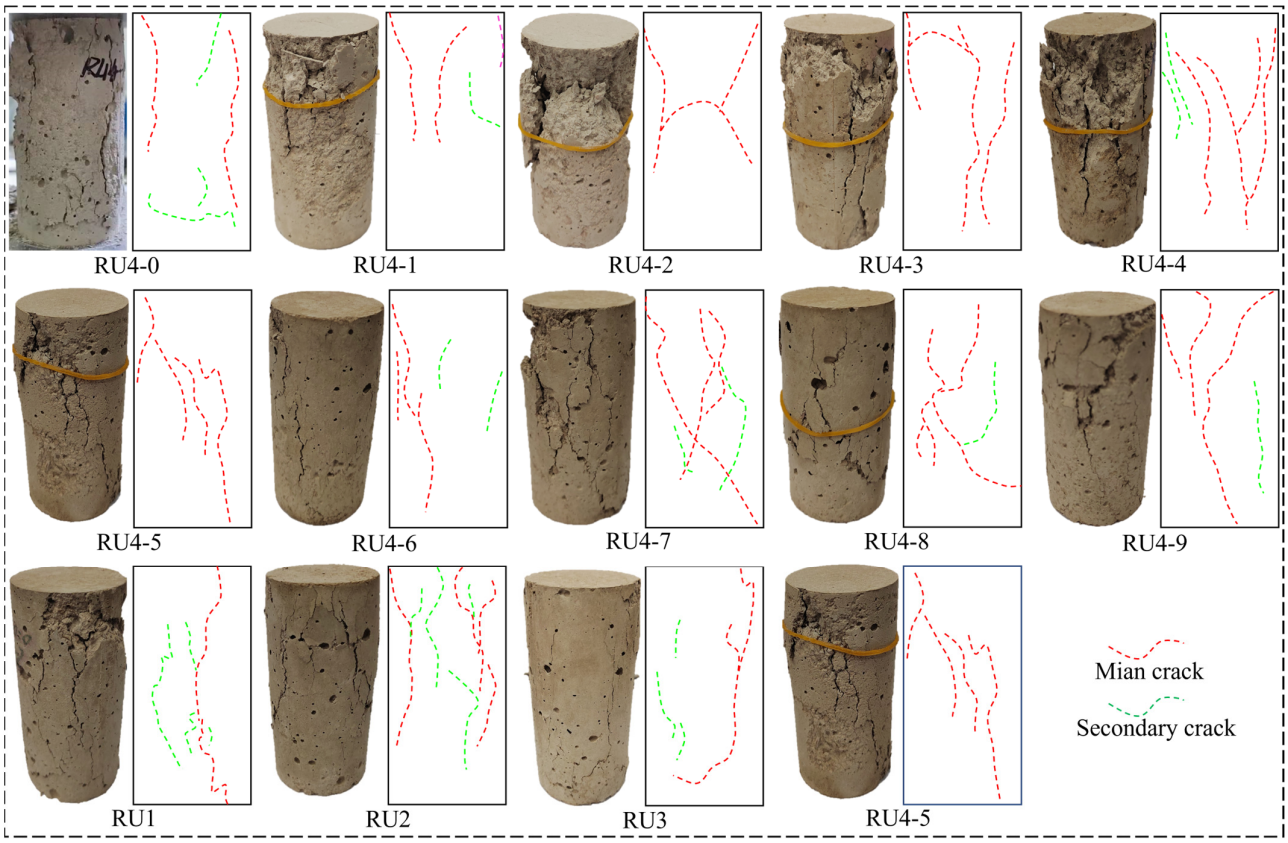

Figure 8. Failure characteristics of CPB samples (RU4-0~9 and RU1~3).

The uniaxial compression failure modes of CPB with different composite binder ratios under five wetting–drying cycles are shown in Figure 8. For sample RU1, with a composite cementing material ratio of 10:0:0, under axial stress loading, a main crack began to gradually expand along the loading direction, accompanied by many secondary cracks. The direction of the secondary crack was roughly parallel to the direction of the axial stress. As the stress value continued to increase, a small piece of debris spalled off at the end of the sample, and the main crack eventually penetrated the entire sample until the entire sample was destabilized. In the process of axial stress loading, sample RU2 with a ratio of 8:0:2 of the composite cementing material produced multiple main cracks and gradually penetrated the middle and lower sides of the sample; the secondary cracks were more developed. The lateral expansion of the sample was obvious, and only a small amount of debris fell, showing ∧-type shear failure. Sample RU3, with a composite cementing material ratio of 8:2:0, produced only one main crack after the sample was destroyed. The main crack gradually expanded from top to bottom, and some secondary cracks were generated locally. The failure characteristics of RU4-5 with a composite cementing material ratio of 8:1:1 are analyzed in Figure 8.

3.2.3. Variation in Cementation Strength

(1) Effects of wetting–drying cycles on UCS and EM

The UCS and EM changes in CPB under different numbers of wetting–drying cycles are shown in Figure 9a,b. The wetting–drying cycling had a significant effect on the UCS and EM. As the number of wetting–drying cycles increased, the UCS and EM decreased exponentially. In zero–five wetting–drying cycles, the UCS decreased by 0.91 MPa, 2.9 MPa,

4.21 MPa, 5.58 MPa and 5.84 MPa, respectively, and the EM decreased by 0.28 GPa, 0.45 GPa, 0.59 GPa, 0.72 GPa and 0.76 GPa, respectively. For zero–four cycles, the wetting–drying cycles had a significant effect on the UCS and EM, and the EM changed the most after the first wetting–drying cycle. The degree of deterioration of CPB by a wetting–drying cycle first increased and then decreased and then increased and decreased, gradually reaching a stable trend. The degradation degree of the UCS under two–four wetting–drying cycles was 21.47%, 18.05% and 22.87%, respectively, and the average degradation degree was 20.80%. Among them, the degradation degree due to the fourth cycle was the largest observed, the rest of the degradation degrees were below 9.27% and the average degradation degree of the UCS under five–ten wetting–drying cycles was 7.53%. This shows that two–four wetting–drying cycles had a great influence on the UCS, among which the fourth wetting–drying cycle had the greatest degree of deterioration, and the five–ten wetting–drying cycles had a relatively stable degree of deterioration. The degree of deterioration of the EM for two–four wetting–drying cycles was 28.12%, 23.89%, 25.71% and 32.50%, respectively, and the average degree of deterioration was 27.56%. Among them, the fourth wetting–drying cycle had the greatest degree of EM deterioration, and the remaining degrees of deterioration were below 13.37%, indicating that zero–four wetting–drying cycles had a significant impact on the deterioration of the EM, and the average degree of deterioration of the EM was greater than that of the UCS, indicating that the EM was more sensitive to wetting–drying cycles than the UCS.

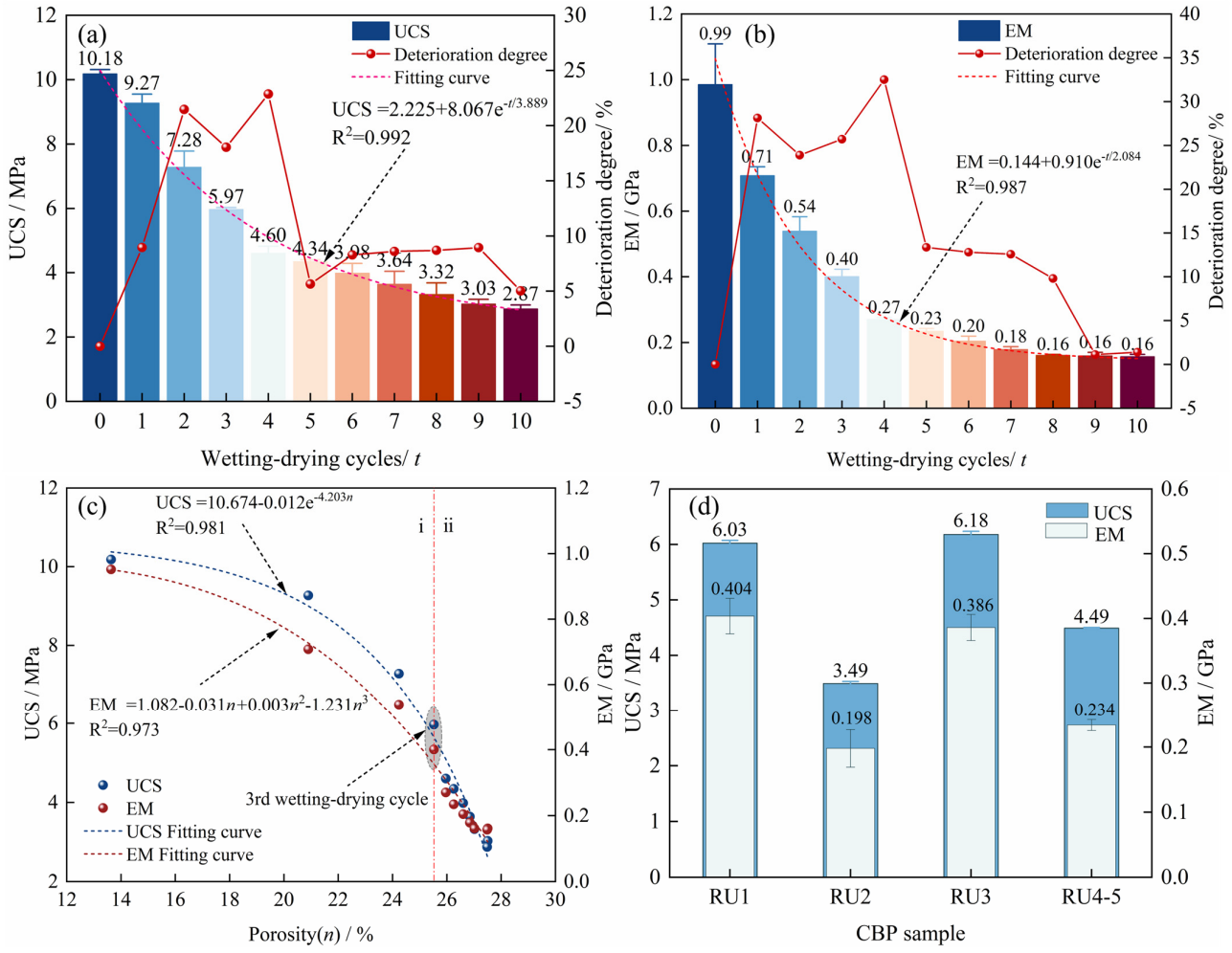

Figure 9. (**a**,**b**) The changes in and deterioration degrees of UCS and EM with wetting–drying cycles, respectively. (**c**) The relationship between UCS, EM and porosity. (**d**) Effect of different cementing materials on CPB strength.

(2) Variation in UCS and EM with porosity

To further analyze the relationship between UCS and EM and porosity, Figure 9c was drawn. The UCS decreased exponentially with increasing porosity n. However, the EM decreased in the form of a quadratic function with increasing porosity n. According to the rate of change in the UCS and EM curves with porosity, these curves were roughly divided into an initial deterioration stage i and a secondary deterioration stage ii. In the initial deterioration stage i, UCS and EM decreased slowly with increasing porosity, indicating that the porosity had little effect on the UCS and EM at this stage. In the secondary deterioration stage ii, with the increase in porosity, the change rate of the UCS and EM curves was accelerated, indicating that the porosity had a significant effect on the UCS and EM.

(3) The change in CPB bond strength of different composite cementing materials

Figure 9d shows that the CPB bond strengths of composite cementitious materials with different contents after five wetting–drying cycles were quite different. The average UCS results of RU1 and RU3 were 6.03 MPa and 6.18 MPa, respectively. The average UCS results of RU2 and RU4-5 were 3.49 MPa and 4.49 MPa, respectively. The average UCS results of RU1 and RU3 (6.11 MPa) were higher than the 75.07% and 36.08% of RU2 and RU4-5, respectively. The average EM results of RU1 and RU3 (0.395 GPa) were higher than those of RU2 and RU4-5 by 99.49% and 68.80%, respectively. The UCS and EM of the RU1 and RU3 series of samples with ratios of 10:0:0 and 8:2:0 were similar and higher, and the UCS and EM of the RU2 and RU4 series of samples with ratios of 8:0:2 and 8:1:1 were lower. The CPB strength of the four composite cementing materials followed the order of RU1 ≈ RU3 > RU4-5 > RU2.

3.3. Damage Evolution

According to the experimental data of the stress–strain curves of CPB samples under different numbers of wetting–drying cycles in the UCS test, the strain values (peak strain) corresponding to UCS, EM and UCS were obtained. The physical and mechanical parameters m and $1/m$ of CPB samples were obtained by substituting them into Equation (13), and the CPB damage constitutive equation was calculated, as shown in Table 2.

Table 2. Parameter value and equation of the damage constitutive model for marl paste samples.

Sample Number	EM/MPa	UCS/MPa	Strain ε	m	$1/m$	Damage Constitutive Equation
RU4-0-1	1009.16	10.225	0.0159	2.223	0.450	$\sigma = 1009.16\varepsilon \exp\left(-0.450(\varepsilon/0.0159)^{2.223}\right)$
RU4-2-1	469.73	6.666	0.0182	4.069	0.246	$\sigma = 496.73\varepsilon \exp\left(-0.246(\varepsilon/0.0182)^{4.069}\right)$
RU4-4-1	286.97	4.723	0.0228	3.055	0.327	$\sigma = 286.97\varepsilon \exp\left(-0.327(\varepsilon/0.0228)^{3.055}\right)$
RU4-6-1	203.61	4.149	0.0284	3.073	0.325	$\sigma = 203.61\varepsilon \exp\left(-0.325(\varepsilon/0.0284)^{3.073}\right)$
RU4-8-1	160.52	3.519	0.0314	2.781	0.360	$\sigma = 160.52\varepsilon \exp\left(-0.360(\varepsilon/0.0314)^{2.781}\right)$
RU4-10-1	112.66	2.951	0.0359	3.185	0.314	$\sigma = 112.66\varepsilon \exp\left(-0.314(\varepsilon/0.0359)^{3.185}\right)$

The parameters in Table 2 were brought into Equation (15) to obtain the damage variable evolution curves of CPB samples under different wetting–drying cycles, as shown in Figure 10. There were significant differences in D_W for different wetting–drying cycles. As the number of wetting–drying cycles increased, D_W increased. In general, compared with CPB samples without wetting–drying cycles, the influence of the first three wetting–drying cycles were the largest for D_W, and the values were between 0 and 0.562. The D_W variation during four–ten wetting–drying cycles was relatively small, and its value was between 0.716 and 0.888. The damage accumulation of the CPB sample gradually slowed, namely, the axial strain gradually increased. The damage variable of the CPB sam-

ple reached one in a large strain range. The evolution curve of the total damage variable showed an S shape and was divided into four stages (taking CPB samples without wetting–drying cycles as an example). The initial damage stage I: there were microcracks in the CPB at this stage, and the microcracks gradually closed under uniaxial loading. In a small strain range, the CPB remains. Accelerated damage propagation stage II: in this stage, with the increase in the load, the microcracks inside the CPB developed rapidly, resulting in the dislocation and connection of pores and cavities; the total damage value increased rapidly, and the CPB peak strength was reached. Damage decelerated propagation stage III: the microcracks and voids inside the CPB were connected, so that the CPB gradually lost its bearing capacity, and the total damage value gradually approached one. End of damage stage IV: the CPB internal cracks broke through to the surface, and the CPB completely lost its bearing capacity, so the total damage value remained unchanged at one.

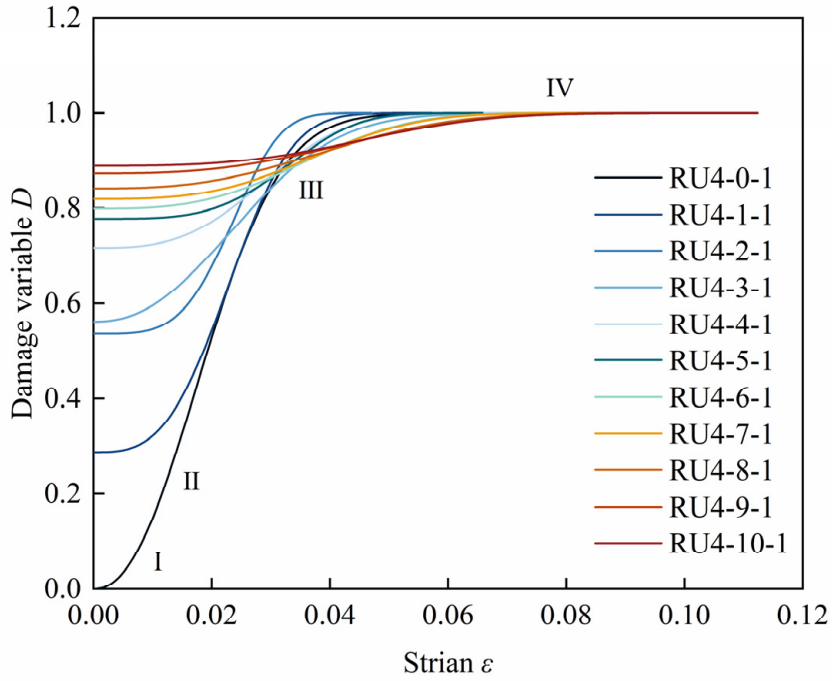

Figure 10. Damage variable curve of CPB samples.

The parameters in Table 2 were brought into Equation (16) to obtain the damage constitutive equation of CPB under different wetting–drying cycles. According to the damage constitutive equation, the theoretical prediction curve and the measured curve were drawn, as shown in Figure 11. It can be seen from the figure that the theoretical prediction curve is in good agreement with the measured curve, which indicates that the established damage constitutive model is reasonable and reliable and can provide a reference for the CPB filling design of open-pit mines.

3.4. Deterioration Mechanism of the Microstructure

For CPB samples under zero–four wetting–drying cycles, small pores developed, and the overall structure was relatively dense. The internal hydration products of the CPB were analyzed. As the number of wetting–drying cycles increased, the number of ettringite grains with longer needle bar lengths increased, and the remaining hydration products remained basically unchanged. Compared with CPB samples without wetting–drying cycles, small particles fell off of the surface of the CPB internal cement during the second and fourth wetting–drying cycles, as shown in Figure 12a–c. For the CPB samples that underwent 8 and 10 cycles, the surface voids of the cement were more developed, the traces of large particles falling off were obvious, many small cracks appeared and the structure of the cement was seriously damaged, but the cement still maintained a large structure.

Large cracks appeared along the edge of the aggregate, the connection between the cement and the aggregate was poor and the whole sample was in a loose state. The number of internal ettringite was small, and the calcium silicate hydrate (C-S-H) distribution gradually changed from a network distribution to a coral and cluster distribution. The spherical contour of aluminum glue gradually became obvious, the internal macropores were well connected and the porosity was relatively large, as shown in Figure 12d–f.

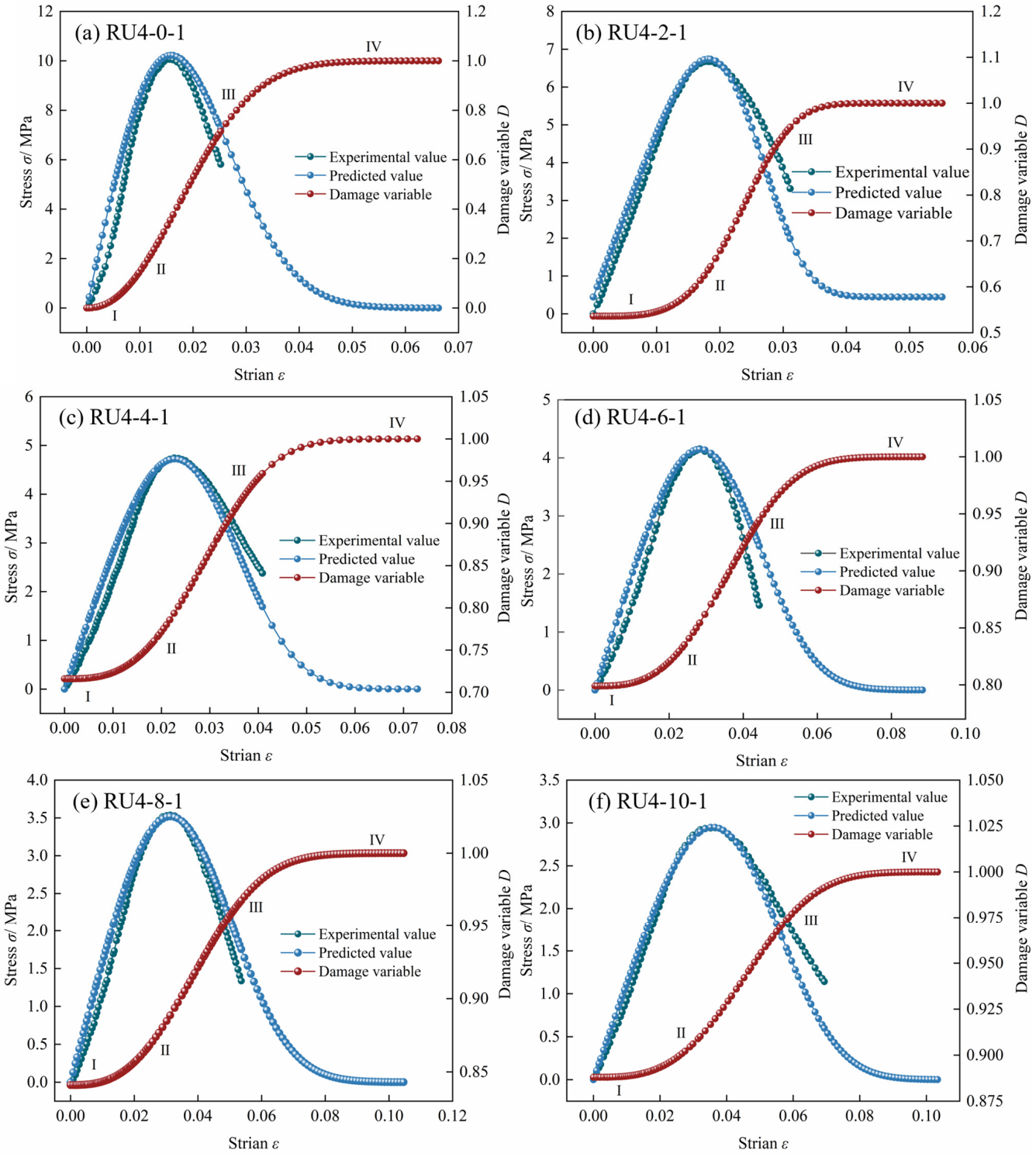

Figure 11. Stress-strain test and theoretical curve and damage variable curve of CPB samples. I is initial damage stage, II is accelerated damage propagation stage, III is damage decelerated propagation stage and IV is end of damage stage (**a**–**f**).

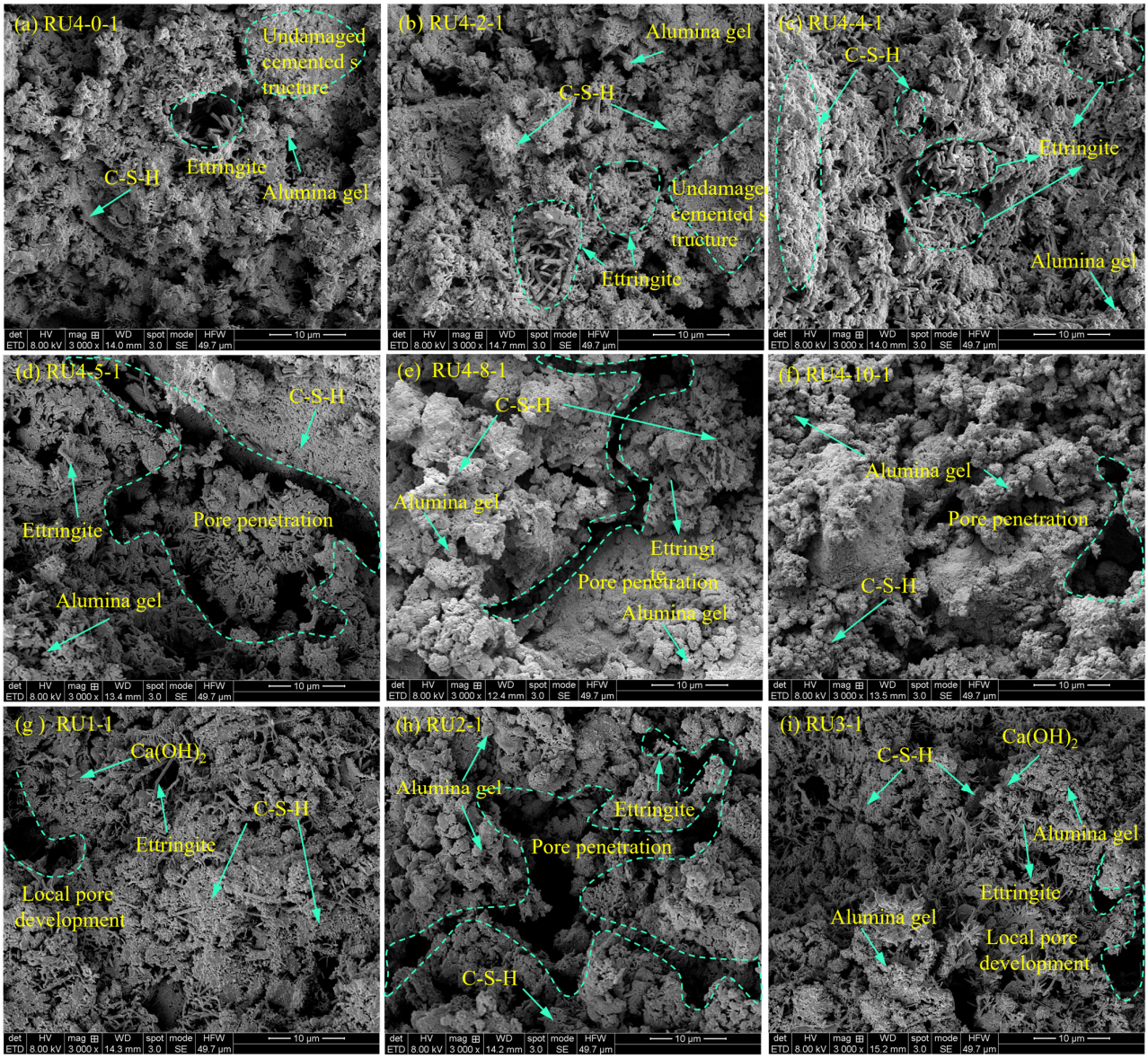

Figure 12. SEM images of CPB samples.

From the comparison of the density of CPB samples, RU1-1 and RU3-1 were denser, followed by RU4-5-1, and RU2-1 was the worst. Regarding the development of microcracks on the surface of the cement, RU2-1 and RU4-5-1 developed well, and RU1-1 and RU3-1 had a low degree of microcrack propagation. The damage degrees of the cement followed the order of RU2-1 > RU4-5-1 > RU1-1, RU3-1. Comparing the quantity and structure of the hydration products, the quantity of ettringite followed the order of RU1-1, RU3-1 > RU4-5-1 > RU2-1. For RU2-1 > RU4-5-1 > RU1-1, RU3-1, RU2-1 and RU4-5-1, the macropores gradually penetrated, whereas for RU1-1 and RU3-1, local pores penetrated, as shown in Figure 12d,g,h.

4. Discussion

The common methods for recovering coal resources in the highwall of open-pit coal mines include continuous miner highwall mining [52], timeliness slope theory [63], steep end-slope mining [64] and filling roadway mining [65]. Timeliness slope theory and steep end-slope mining technology further increase the mining angle of the slope and complete the coal mining of the limit mining angle of the highwall within a certain period but cannot solve the problem of coal mining under the highwall [66]. The filling roadway mining

technology of highwall roadways overcomes the limit of steep end-slope mining technology, but it is restricted according to the relevant national regulations and mining costs [67]. At present, continuous miner highwall mining is used to mine near-horizontal and gently inclined coal seams in the highwall, and many coal pillars are retained, making the recovery rate of the coal resources less than 50% [51]. Therefore, based on the technology of continuous highwall mining of the overlying coal seam under the highwall, the waste is used as CPB aggregate to backfill the adit (Figure 4a) to realize the utilization of solid waste and the recovery of coal resources with maximum efficiency. To better realize the concept of ecological restoration during mining and reclamation [68], in the integrated collaborative operation of stripping–mining–transportation–filling/dumping–reclamation in open-pit mines (Figure 4b), it is necessary to emphasize the coordination, cooperation and synchronization among various mining processes and reclamation processes. The synergistic attributes and the synergistic effects generated reflect the spatiotemporal relationship among the stripping, mining, transportation, filling, dumping and reclamation projects in open-pit mines. An orderly design considering time, space and level is established, and unified planning and parallel operation are carried out to form a process system of collaborative mining of the same open-pit mine, the coordinated disposal of solid waste and common reclamation.

A wetting–drying cycle had a significant effect on the physical and macroscopic mechanical properties of CPB. In a wetting–drying cycle, CPB samples produced a certain number of microcracks and cracks, as shown in Figure 5a–k. This was because there was no water bonding on the surface of a CPB sample, but there was a temperature difference between the inside and outside of the sample, resulting in thermal expansion and contraction. The surface of the sample lost water quickly, and the surface tension was less than the internal tension. Under the combined action of gravity and tension at the bottom of the sample, many microcracks were generated. With the increase in the number of wetting–drying cycles, the position of microcracks on the surface of CPB samples was continuously damaged by wetting–drying cycles, resulting in the water–rock chemical reaction of clay minerals and gypsum on the surface, so that microcracks gradually expanded into cracks [26]. The main reason for the cracks in Figure 5l–s was that the greater the proportion of gypsum in the CPB samples, the greater the promoting effect of temperature on the formation of ettringite [69]. The greater the number of wetting–drying cycles, the higher the probability of expansion of the ettringite in the sample, which caused the internal stress in the CPB samples to expand and crack the original skeleton of the sample, resulting in expansion cracking [70,71]. With the development of microcracks and cracks on the surface of CPB samples, gypsum aggravates the propagation of cracks, which is extremely unfavorable to the integrity of the samples.

According to past research on cementing materials under wetting–drying cycles, the main reasons for the deterioration of CPB in stage i are the loss of small particles from the CPB skeleton, the water–rock chemical reactions of clay minerals and the development of microcracks and cavities. CPB is formed by the consolidation and demolding of particles with different sizes as aggregates under the hydration reaction of composite cementitious materials. Among them, particles with particle sizes less than 0.3 mm account for 13.93%, which form noncritical cements with composite cementing materials [22] and fill the spaces between larger particles. During a drying–wetting cycle, these noncritical cements are destroyed, and small particles are detached from the cements [72] and are transported to the distilled water through pores and microcrack channels, resulting in noncritical cements. A loose, weak cementation ability can also be observed in Figure 12a–c. According to the mineral composition analysis of marl, it contains 24.50% clay minerals, and these clay minerals include illite (44%), illite–smectite mixed-layer minerals (36%) and kaolinite (20%), as shown in Figure 2. Illite and illite–smectite mixed-layer minerals are highly hydrophilic minerals [24]. During the immersion process, it was found that the color of the distilled water mixture gradually turned pale yellow after immersion, which was speculated to be caused by the loss of the water–rock chemical reaction from illite and illite–smectite

mixed-layer minerals to distilled water [32]. This phenomenon caused the disintegration of illite and illite–smectite mixed-layer minerals, a loss of connection between clay particles or between clay particles and noncritical cements [37], the expansion of noncritical cements and an increase in noncritical cement pores [29]. Under the action of wetting–drying cycles, the clay particles repeatedly underwent expansion–contraction or even disintegration (the process mechanism is shown in Figure 13), until they detached from the cement. Under the action of water gravity, the water carried small particles, such as detached clay particles, flowing from the pores and initial microcracks [73], resulting in the loss of some fine aggregate particles inside the CPB before the four wetting–drying cycles. In addition to the weakening of the cementation ability of the noncritical cements, the microcracks and voids generated inside the CPB during the consolidation and demolding process still dominated the mechanical failure performance of the first three wetting–drying cycles [31,60].

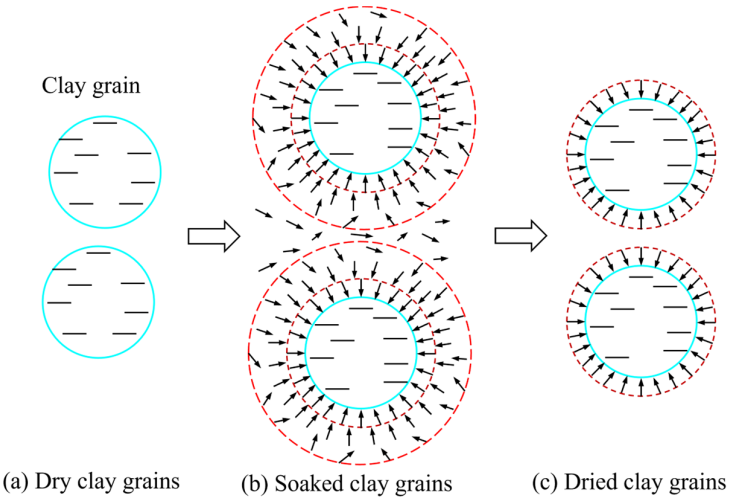

Figure 13. Clay grain expansion process of cement.

In the degradation stage (stage ii), the loss of small particles, clay minerals and cements in the CPB decreased, and its UCS and EM decreased rapidly. Because cement is the main component of CPB, it is mainly the hydration product of the composite binder [74]. As the number of wetting–drying cycles increases, the hydration products in the cement at the critical steady state frequently undergo a water absorption–dehydration process, and these hydration products are easily converted at a certain [75]. When the ettringite growth reaches a certain level, at temperatures above 65 °C, some of the ettringite will decompose to form delayed ettringite [76]. When the temperature reaches 95 °C, the ettringite will disappear quickly and become difficult to observe [69]. Some other ettringite absorbs a large amount of water molecules, causing repulsion between the particles, resulting in expansion [77] and causing the cement in the critical stable state to be destroyed (Figure 12d–f), resulting in an increase in the number of internal cracks in the CPB and the gradual development of microcracks. Finally, although the number of wetting–drying cycles increased, the UCS and EM basically remained stable, indicating that the key cements and aggregates in the CPB form a relatively stable skeleton [22] and are not easily affected by wetting–drying cycles.

CPB with composite cementitious ordinary Portland cement and sulfoaluminate cement has better resistance to the deterioration of wetting–drying cycles, while CPB with gypsum has poor water resistance (Figure 5l–s) (Durgun, 2020), and the more gypsum that is added, the less stable the strength of CPB (Figure 9d). From the variation in UCS and EM, EM is more sensitive to gypsum incorporation than UCS. Although some hydration products in CPB with normal Portland cement and sulfoaluminate cement are degraded, they still maintain a relatively complete cementation structure, so they can maintain a higher UCS and EM. However, too much ettringite may be generated in CPB with too much added gypsum [78], which accelerates the development of pores and microcracks

and destroys the bonding structure (Figure 12g–i), resulting in a weakened resistance to deformation and decreased compression resistance.

There were significant differences in D_W between different wetting–drying cycles, and D_W increased with an increasing number of wetting–drying cycles [79]. With the increase in axial strain, the total damage variable evolution curve of CPB presented an 'S' shape, and Song et al. [80] and Wang et al. [41]) also obtained this conclusion. CPB deformation to failure is a progressive damage process [81].

Based on the above, for the CPB backfill of open-pit coal mines with frequent groundwater activities and frequent rainfall, especially backfill with aggregates with a high clay mineral content, it is necessary to strengthen waterproofing and drainage measures. The upper bench of the adit is also protected by a flood dam, and flood protection is provided at the adit entrance to ensure that surface precipitation does not enter the adit and affect the stability of the coal pillar, the filling body and the roof of the adit. The exposed areas of the filled adit are protected by sprayed concrete to minimize the deterioration of the filling body wetting–drying cycles weathering. Carefully consider the amount of gypsum added, and pay attention to CPB softening in water to prevent slope failure due to the deterioration of the physical and mechanical properties of the CPB and weak layer sliding.

5. Conclusions

(1) The highwall filling mining method and the stripping–mining–transportation–filling/dumping–reclamation integrated operation scheme are proposed to achieve solid waste utilization and improve the recovery rate of coal resources in an open-pit coal mine.

(2) The wetting–drying cycles and added gypsum accelerated the development of microcracks and cracks on the CPB surface. The higher the gypsum content, the further developed the microcracks and cracks on the surface of the CPB after five wetting–drying cycles, which was not conducive to the strength stability of CPB, and EM was more sensitive to gypsum incorporation than UCS.

(3) With the increase in the number of wetting–drying cycles, the porosity increased gradually and tended to be stable after four cycles. The tested CPB showed ductile failure. The crack coalescence form of the CPB during the 0–3 wetting–drying cycles was shear and tensile coalescence, and that during the 4–10 cycles was shear coalescence. Both UCS and EM decreased exponentially with the increase in the number of wetting–drying cycles, but they decreased exponentially and cubically, respectively, with the increase in porosity.

(4) The initial degradation stage of the CPB was caused by the loss of small particulate matter from the skeleton, the water–rock chemical reaction of clay minerals and the development of original microcracks and cavities. The main reason for the secondary deterioration stage was the destruction of the cement in the critical stable state formed by the hydration products.

(5) With the increase in the number of wetting–drying cycles, the initial damage degree of the CPB increased continuously. The damage to the CPB during the zero–three wetting–drying cycles was the largest observed, and the evolution curve of the total damage variable showed an 'S' shape. The proposed damage constitutive model of CPB is reasonable and reliable and can provide a reference for CPB filling design in open-pit coal mines.

Author Contributions: Conceptualization, T.C.; Methodology, T.C.; Software, J.L.; Validation, J.S.; Formal analysis, J.S.; Investigation, Z.T.; Resources, Z.T.; Data curation, L.H.; Writing—original draft, L.H.; Writing—review & editing, J.L.; Visualization, Z.T.; Supervision, L.H.; Funding acquisition, J.S. All authors have read and agreed to the published version of the manuscript.

Funding: This research was funded by the National Natural Science Foundation of China grant number 51774271 And and the National Natural Science Foundation of China Youth Fund Project grant number 51804298.

Data Availability Statement: The data presented in this study are available on request from the corresponding author. The data are not publicly available due to reduce the length of paper.

Acknowledgments: We are grateful to the anonymous reviewers for their valuable suggestions in improving the manuscript.

Conflicts of Interest: Author Tan, Z. was employed by the company Yunnan·Top Field-Mining Sci & Tech., Ltd. The remaining authors declare that the research was conducted in the absence of any commercial or financial relationships that could be construed as a potential conflict of interest.

Appendix A

Table A1. Physical properties of marl after crushing.

Numbering	Particle Size Distribution (mm)					Fractal Dimension FD	Match Index R^2
	<0.300	0.300–0.600	0.600–1.180	1.180–2.360	2.360–4.750		
1	13.93	7.04	11.44	11.62	55.97	2.40	0.947
2	11.40	13.18	14.56	10.48	50.38	2.34	0.986
3	12.41	9.73	13.87	11.56	52.43	2.36	0.979
4#	11.34	11.32	12.16	18.87	46.31	2.37	1.000

Table A2. Key parameters of X'Pert Pro MPD.

Model	X'Pert Pro MPD
Manufacturer	Nalytical, Netherlands
X-ray tube	Copper target
Maximum power	2.2 kW
Maximum tube voltage	60 kV
Maximum tube current	55 mA
Diffraction angle	1°~160°

Appendix B

Table A3. Chemical composition statistics of marl (%).

Sample	CaO	SiO_2	Al_2O_3	Fe_2O_3	MgO	K_2O	TiO_2	SO_3	Other
Marl	39.78	33.23	14.76	5.90	2.50	2.22	0.70	0.62	0.29

Table A4. Chemical composition statistics of normal Portland cement (%).

Sample	CaO	SiO_2	Al_2O_3	SO_3	Fe_2O_3	MgO	Ignition Loss
Normal portland cement	49.70	22.60	9.87	3.84	3.50	2.06	8.43

Table A5. Statistics of chemical composition of sulphate aluminum cement (%).

Sample	CaO	Al_2O_3	SO_3	SiO_2	Fe_2O_3	MgO	TiO_2	Ignition Loss
Sulphatealuminium cement	45.30	18.40	12.50	7.23	4.30	1.35	0.87	10.05

Table A6. Chemical composition statistics of gypsum (%).

Sample	SO_3	CaO	Al_2O_3	SiO_2	Fe_2O_3	SrO
gypsum	59.92	39.76	0.13	0.11	0.04	0.04

Table A7. Key parameters of electric blast drying oven.

Model	HS-DHG-9070A
Power supply voltage	AC220V ± 10%, 50 Hz ± 1 Hz
Heating power	1050 W
Working temperature	Room temperature~200 °C
Temperature control accuracy	±0.1 °C
Timing device	0~9999 h

Table A8. Key parameters of Scanning Electron Microscope.

Model	FEI-QUANTA-FEG 250
Resolution	1.04 nm
Magnification	15~300,000
Accelerating voltage	0.2~30 kV
Searching current	0.3–22 nA

Appendix C

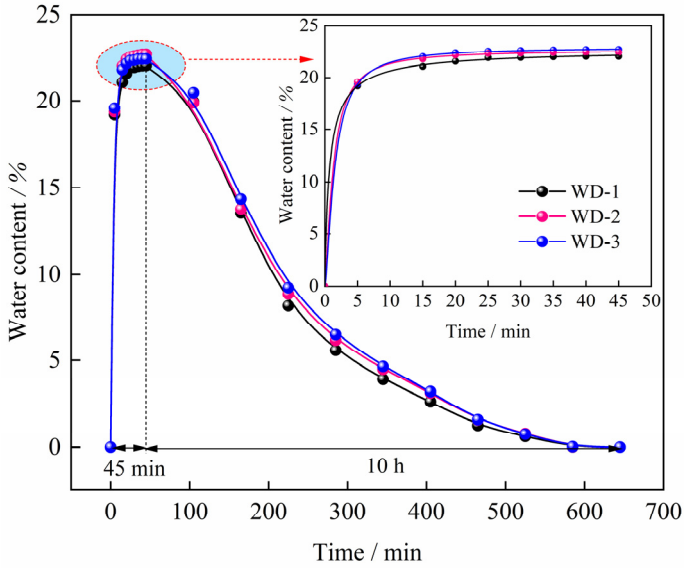

Figure A1. Variation in the water content of marl paste samples with time.

References

1. Li, M.; Zhang, J.; Li, A.; Zhou, N. Reutilisation of coal gangue and fly ash as underground backfill materials for surface subsidence control. *J. Clean. Prod.* **2020**, *254*, 120113. [CrossRef]
2. Cheng, W.; Lei, S.; Bian, Z.; Zhao, Y.; Li, Y.; Gan, Y. Geographic distribution of heavy metals and identification of their sources in soils near large, open-pit coal mines using positive matrix factorization. *J. Hazard. Mater.* **2020**, *387*, 121666. [CrossRef]
3. Li, J.; Yan, X.; Cao, Z.; Yang, Z.; Liang, J.; Ma, T.; Liu, Q. Identification of successional trajectory over 30 Years and evaluation of reclamation effect in coal waste dumps of surface coal mine. *J. Clean. Prod.* **2020**, *269*, 122161. [CrossRef]
4. Rodríguez-Galán, M.; Baena-Moreno, F.M.; Vázquez, S.; Arroyo-Torralvo, F.; Vilches, L.F.; Zhang, Z. Remediation of acid mine drainage. *Environ. Chem. Lett.* **2019**, *17*, 1529–1538. [CrossRef]
5. Porsani, J.L.; de Jesus, F.A.N.; Stangari, M.C. GPR Survey on an Iron Mining Area after the Collapse of the Tailings Dam I at the Córrego do Feijão Mine in Brumadinho-MG, Brazil. *Remote. Sens.* **2019**, *11*, 860. [CrossRef]
6. Weiler, J.; Firpo, B.A.; Schneider, I.A. Technosol as an integrated management tool for turning urban and coal mining waste into a resource. *Miner. Eng.* **2020**, *147*, 106179. [CrossRef]
7. Pappas, D.M.; Vallejo, L.E. The settlement and degradation of nondurable shales associated with coal mine waste embankments. *Int. J. Rock Mech. Min. Sci.* **1997**, *34*, 241. [CrossRef]
8. Karimaei, M.; Dabbaghi, F.; Sadeghi-Nik, A.; Dehestani, M. Mechanical performance of green concrete produced with untreated coal waste aggregates. *Constr. Build. Mater.* **2020**, *233*, 117264. [CrossRef]

9. Kua, T.-A.; Arulrajah, A.; Horpibulsuk, S.; Du, Y.-J.; Shen, S.-L. Strength assessment of spent coffee grounds-geopolymer cement utilizing slag and fly ash precursors. *Constr. Build. Mater.* **2016**, *115*, 565–575. [CrossRef]
10. Amir, M.; Morteza, R. Application of coal waste powder as filler in hot mix asphalt. *Constr. Build. Mater.* **2014**, *66*, 476–483. [CrossRef]
11. Taha, Y.; Benzaazoua, M.; Hakkou, R.; Mansori, M. Coal mine wastes recycling for coal recovery and eco-friendly bricks production. *Miner. Eng.* **2017**, *107*, 123–138. [CrossRef]
12. Weiler, J.; Firpo, B.; Schneider, I. Coal waste derived soil-like substrate: An opportunity for coal waste in a sustainable mineral scenario. *J. Clean. Prod.* **2018**, *174*, 739–745. [CrossRef]
13. Sobolczyk-Bednarek, J.; Choińska-Pulit, A.; Łaba, W. Biosolubilization of low-rank coal by the newly isolated strain *Streptomyces fulvissimus* K59. *Fuel* **2021**, *301*, 121082. [CrossRef]
14. Skripkina, T.; Bychkov, A.; Tikhova, V.; Smolyakov, B.; Lomovsky, O. Mechanochemically oxidized brown coal and the effect of its application in polluted water. *Environ. Technol. Innov.* **2018**, *11*, 74–82. [CrossRef]
15. Mo, S.; Canbulat, I.; Zhang, C.; Oh, J.; Shen, B.; Hagan, P. Numerical investigation into the effect of backfilling on coal pillar strength in highwall mining. *Int. J. Min. Sci. Technol.* **2018**, *28*, 281–286. [CrossRef]
16. Anwar, R.; Ahmed, M.; Seats, P.; Huang, Q.; Lin, L.-S. Prospect of utilizing coal mine drainage sludge as an iron source for value-creating applications. *Rev. Environ. Sci. Bio./Technol.* **2021**, *20*, 679–695. [CrossRef]
17. Kefeni, K.K.; Msagati, T.M.; Maree, J.P.; Mamba, B.B. Metals and sulphate removal from acid mine drainage in two steps via ferrite sludge and barium sulphate formation. *Miner. Eng.* **2015**, *81*, 79–87. [CrossRef]
18. Yuan, L.; Zhang, T.; Zhao, Y.; Ren, B.; Hao, X.; Xu, C. Precise coordinated mining of coal and associated resources: A case of environmental coordinated mining of coal and associated rare metal in Ordos basin. *Zhongguo Kuangye Daxue Xuebao/J. China Univ. Min. Technol.* **2017**, *46*, 449–459. [CrossRef]
19. El Kamash, W.; El Naggar, H.; Nagaratnam, S. Novel adaptation of Marston's stress solution for inclined backfilled stopes. *Alex. Eng. J.* **2022**, *61*, 8221–8239. [CrossRef]
20. Chen, T.; Shu, J.; Han, L.; Tian, G.; Yang, G.; Lv, J. Modeling the effects of topography and slope gradient of an artificially formed slope on runoff, sediment yield, water and soil loss of sandy soil. *Catena* **2022**, *212*, 106060. [CrossRef]
21. Eang, K.E.; Igarashi, T.; Kondo, M.; Nakatani, T.; Tabelin, C.B.; Fujinaga, R. Groundwater monitoring of an open-pit limestone quarry: Water-rock interaction and mixing estimation within the rock layers by geochemical and statistical analyses. *Int. J. Min. Sci. Technol.* **2018**, *28*, 849–857. [CrossRef]
22. Ma, D.; Kong, S.; Li, Z.; Zhang, Q.; Wang, Z.; Zhou, Z. Effect of wetting-drying cycle on hydraulic and mechanical properties of cemented paste backfill of the recycled solid wastes. *Chemosphere* **2021**, *282*, 131163. [CrossRef]
23. Jiang, X.; Li, C.; Zhou, J.-Q.; Zhang, Z.; Yao, W.; Chen, W.; Liu, H.-B. Salt-induced structure damage and permeability enhancement of Three Gorges Reservoir sandstone under wetting-drying cycles. *Int. J. Rock Mech. Min. Sci. Géoméch. Abstr.* **2022**, *153*, 105100. [CrossRef]
24. Kühnel, R.A.; Van der Gaast, S.J.; Broekmans, M.A.; Theng, B.K. Wetting-induced layer contraction in illite and mica-family relatives. *Appl. Clay Sci.* **2017**, *135*, 226–233. [CrossRef]
25. Cheng, Q.; Guo, Y.; Dong, C.; Xu, J.; Lai, W.; Du, B. Mechanical Properties of Clay Based Cemented Paste Backfill for Coal Recovery from Deep Mines. *Energies* **2021**, *14*, 5764. [CrossRef]
26. Aldaood, A.; Bouasker, M.; Al-Mukhtar, M. Impact of wetting–drying cycles on the microstructure and mechanical properties of lime-stabilized gypseous soils. *Eng. Geol.* **2014**, *174*, 11–21. [CrossRef]
27. Durgun, M.Y. Effect of wetting-drying cycles on gypsum plasters containing ground basaltic pumice and polypropylene fibers. *J. Build. Eng.* **2020**, *32*, 101801. [CrossRef]
28. Li, W.; Yi, Y.; Puppala, A.J. Effects of curing environment and period on performance of lime-GGBS-treated gypseous soil. *Transp. Geotech.* **2022**, *37*, 100848. [CrossRef]
29. Ying, Z.; Benahmed, N.; Cui, Y.-J.; Duc, M. Wetting-drying cycle effect on the compressibility of lime-treated soil accounting for wetting fluid nature and aggregate size. *Eng. Geol.* **2022**, *307*, 106778. [CrossRef]
30. Zhou, W.; Cheng, J.; Zhang, G.; Li, H.; Cheng, Y.; Ma, G.; Ji, X. Effects of wetting–drying cycles on the breakage characteristics of slate rock grains. *Rock Mech. Rock Eng.* **2021**, *54*, 6323–6337. [CrossRef]
31. Cantón, Y.; Solé-Benet, A.; Queralt, I.; Pini, R. Weathering of a gypsum-calcareous mudstone under semi-arid environment at Tabernas, SE Spain: Laboratory and field-based experimental approaches. *Catena* **2001**, *44*, 111–132. [CrossRef]
32. Jiang, X.; Huang, Q.; Zhang, Z.; Vallejo, L.E.; Chen, X.; Zhao, W.; Deng, H.; Liu, X.; Song, D.; Chen, Z. Influence of Clay Content on Crack Evolution of Clay–Sand Mixture. *Front. Earth Sci.* **2022**, *10*, 915478. [CrossRef]
33. Hua, W.; Dong, S.; Li, Y.; Xu, J.; Wang, Q. The influence of cyclic wetting and drying on the fracture toughness of sandstone. *Int. J. Rock Mech. Min. Sci. Géoméch. Abstr.* **2015**, *78*, 331–335. [CrossRef]
34. Gu, D.; Liu, H.; Gao, X.; Huang, D.; Zhang, W. Influence of Cyclic Wetting–Drying on the Shear Strength of Limestone with a Soft Interlayer. *Rock Mech. Rock Eng.* **2021**, *54*, 4369–4378. [CrossRef]
35. Li, X.; Peng, K.; Peng, J.; Hou, D. Experimental investigation of cyclic wetting-drying effect on mechanical behavior of a medium-grained sandstone. *Eng. Geol.* **2021**, *293*, 106335. [CrossRef]
36. Wang, J.; Fu, J.; Song, W.; Zhang, Y.; Wu, S. Acoustic emission characteristics and damage evolution process of layered cemented tailings backfill under uniaxial compression. *Constr. Build. Mater.* **2021**, *295*, 123663. [CrossRef]

37. Yang, Y.-L.; Zhang, T.; Liu, S.-Y.; Luo, J.-H. Mechanical Properties and Deterioration Mechanism of Remolded Carbonaceous Mudstone Exposed to Wetting–Drying Cycles. *Rock Mech. Rock Eng.* **2022**, *55*, 3769–3780. [CrossRef]
38. Zhang, Z.; Han, L.; Wei, S.; Chen, L.; Liu, G.; Zhang, L. Disintegration law of strongly weathered purple mudstone on the surface of the drawdown area under conditions of Three Gorges Reservoir operation. *Eng. Geol.* **2020**, *270*, 105584. [CrossRef]
39. Aldhafeeri, Z.; Fall, M. Time and damage induced changes in the chemical reactivity of cemented paste backfill. *J. Environ. Chem. Eng.* **2016**, *4*, 4038–4049. [CrossRef]
40. Fu, J.; Wang, J.; Song, W. Damage constitutive model and strength criterion of cemented paste backfill based on layered effect considerations. *J. Mater. Res. Technol.* **2020**, *9*, 6073–6084. [CrossRef]
41. Wang, J.; Zhang, C.; Fu, J.; Song, W.; Zhang, Y. Effect of water saturation on mechanical characteristics and damage behavior of cemented paste backfill. *J. Mater. Res. Technol.* **2021**, *15*, 6624–6639. [CrossRef]
42. Zhou, Y.; Yan, Y.; Zhao, K.; Yu, X.; Song, Y.; Wang, J.; Suo, T. Study of the effect of loading modes on the acoustic emission fractal and damage characteristics of cemented paste backfill. *Constr. Build. Mater.* **2021**, *277*, 122311. [CrossRef]
43. Yin, S.; Hou, Y.; Chen, X.; Zhang, M.; Du, H.; Gao, C. Mechanical behavior, failure pattern and damage evolution of fiber-reinforced cemented sulfur tailings backfill under uniaxial loading. *Constr. Build. Mater.* **2022**, *332*, 127248. [CrossRef]
44. Zhang, C.; Wang, J.; Song, W.; Fu, J. Pore structure, mechanical behavior and damage evolution of cemented paste backfill. *J. Mater. Res. Technol.* **2022**, *17*, 2864–2874. [CrossRef]
45. Wu, J.; Feng, M.; Mao, X.; Xu, J.; Zhang, W.; Ni, X.; Han, G. Particle size distribution of aggregate effects on mechanical and structural properties of cemented rockfill: Experiments and modeling. *Constr. Build. Mater.* **2018**, *193*, 295–311. [CrossRef]
46. Zhou, N.; Zhang, J.; Ouyang, S.; Deng, X.; Dong, C.; Du, E. Feasibility study and performance optimization of sand-based cemented paste backfill materials. *J. Clean. Prod.* **2020**, *259*, 120798. [CrossRef]
47. Mark, C.; Agioutantis, Z. Analysis of coal pillar stability (ACPS): A new generation of pillar design software. *Int. J. Min. Sci. Technol.* **2019**, *29*, 87–91. [CrossRef]
48. Verma, C.P.; Porathur, J.L.; Thote, N.R.; Roy, P.P.; Karekal, S. Empirical Approaches for Design of Web Pillars in Highwall Mining: Review and Analysis. *Geotech. Geol. Eng.* **2014**, *32*, 587–599. [CrossRef]
49. Porathur, J.L.; Karekal, S.; Palroy, P. Web pillar design approach for Highwall Mining extraction. *Int. J. Rock Mech. Min. Sci. Géoméch. Abstr.* **2013**, *64*, 73–83. [CrossRef]
50. Jiang, J.; Lu, Y.; Wang, D.; Han, X. Slope stability calculation method for highwall mining with open-cut mines. *Sci. Rep.* **2022**, *12*, 209. [CrossRef]
51. Ross, C.; Conover, D.; Baine, J. Highwall mining of thick, steeply dipping coal—A case study in geotechnical design and recovery optimization. *Int. J. Min. Sci. Technol.* **2019**, *29*, 777–780. [CrossRef]
52. Adhikary, D.; Shen, B.; Fama, M. A study of highwall mining panel stability. *Int. J. Rock Mech. Min.* **2002**, *39*, 643–659. [CrossRef]
53. Chen, T.; Han, L.; Shu, J. A Filling Mining Method for an End Slope Large-Dip-Angle Thick Coal Seam of a Strip Mine. China Patent No CN202110708279, 25 June 2022.
54. Ke, X.; Zhou, X.; Wang, X.; Wang, T.; Hou, H.; Zhou, M. Effect of tailings fineness on the pore structure development of cemented paste backfill. *Constr. Build. Mater.* **2016**, *126*, 345–350. [CrossRef]
55. Xu, X.; Gao, F.; Zhang, Z. Thermo-mechanical coupling damage constitutive model of rock based on the Hoek–Brown strength criterion. *Int. J. Damage Mech.* **2017**, *27*, 1213–1230. [CrossRef]
56. Han, T.; Shi, J.; Cao, X. Fracturing and Damage to Sandstone Under Coupling Effects of Chemical Corrosion and Freeze–Thaw Cycles. *Rock Mech. Rock Eng.* **2016**, *49*, 4245–4255. [CrossRef]
57. Zhao, Y.; Ran, H.; Feng, G.; Guo, Y.; Fan, Y. Damage evolution and failure characteristics of cemented gangue backfill body with different height-width ratios under uniaxial compression. *Caikuang Yu Anquan Gongcheng Xuebao/J. Min. Saf. Eng.* **2022**, *39*, 674–682. [CrossRef]
58. Wu, X.; Liu, J.; Liu, X.; Zhao, K.; Zhang, Y. Study on the coupled relationship between AE accumulative ring-down count and damage constitutive model of rock. *Caikuang Yu Anquan Gongcheng Xuebao/J. Min. Saf. Eng.* **2015**, *32*, 28–34. [CrossRef]
59. Quennoz, A.; Scrivener, K.L. Interactions between alite and C3A-gypsum hydrations in model cements. *Cem. Concr. Res.* **2013**, *44*, 46–54. [CrossRef]
60. Huan, C.; Zhu, C.; Liu, L.; Wang, M.; Zhao, Y.; Zhang, B.; Zhang, X. Pore Structure Characteristics and Its Effect on Mechanical Performance of Cemented Paste Backfill. *Front. Mater.* **2021**, *8*, 700917. [CrossRef]
61. Zhao, K.; Wu, J.; Yan, Y.; Zhou, Y.; Yang, J.; He, Z. Multi-scale characteristics of crack evolution of cemented tailings backfill. *Yanshilixue Yu Gongcheng Xuebao/Chin. J. Rock Mech. Eng.* **2022**, *41*, 1626–1636. [CrossRef]
62. Bobet, A.; Einstein, H. Fracture coalescence in rock-type materials under uniaxial and biaxial compression. *Int. J. Rock Mech. Min. Sci. Géoméch. Abstr.* **1998**, *35*, 863–888. [CrossRef]
63. Cai, Q.; Zhou, W.; Che, Z.; Liu, Y.; Peng, H. Research on the mining method and stripping ratio of steep end-slope min-ing in surface coal mines with flat coal deposit. *Zhongguo Kuangye Daxue Xuebao/J. China Univ. Min. Technol.* **2007**, *36*, 743–747.
64. Cai, Q.; Zhou, W.; Shu, J.; Liu, Y.; Peng, H. Analysis and application on end-slope timeliness of internal dumping under flat dipping ore body in large surface coal mine. *Zhongguo Kuangye Daxue Xuebao/J. China Univ. Min. Technol.* **2008**, *37*, 740–744.
65. Zhang, Q.; Zhang, J.; Chen, Y.; Ntigurirwa, J.D.; Xia, K. Moving set-up room theory of weakening the mining pressure caused by the backfilling body in solid backfilling mining. *Energy Sci. Eng.* **2020**, *8*, 898–909. [CrossRef]

66. Shang, T.; Han, L.; Shu, J.; Chen, S. Slope structure and stress development rule under mining mode of land saving and ecological detraction. *Meitan Xuebao/J. China Coal Soc.* **2019**, *44*, 3644–3654. [CrossRef]
67. Wang, F.; Zhang, C. Reasonable coal pillar design and remote control mining technology for highwall residual coal resources. *R. Soc. Open Sci.* **2019**, *6*, 181817. [CrossRef]
68. Hu, Z.; Xiao, W.; Zhao, Y. Re-discussion on coal mine eco-environment concurrent mining and reclamation. *Meitan Xuebao/J. China Coal Soc.* **2020**, *45*, 351–359. [CrossRef]
69. Ramlochan, T.; Thomas, M.; Hooton, R. The effect of pozzolans and slag on the expansion of mortars cured at elevated temperature: Part II: Microstructural and microchemical investigations. *Cem. Concr. Res.* **2004**, *34*, 1341–1356. [CrossRef]
70. Ogawa, K.; Roy, D. C4A3S hydration, ettringite formation, and its expansion mechanism: II. Microstructural observation of expansion. *Cem. Concr. Res.* **1982**, *12*, 101–109. [CrossRef]
71. Calvo, J.G.; Carballosa, P.; Pedrosa, F.; Revuelta, D. Microstructural phenomena involved in the expansive performance of cement pastes based on type K expansive agent. *Cem. Concr. Res.* **2022**, *158*, 106856. [CrossRef]
72. Bian, X.; Zhang, W.; Li, X.; Shi, X.; Deng, Y.; Peng, J. Changes in strength, hydraulic conductivity and microstructure of superabsorbent polymer stabilized soil subjected to wetting–drying cycles. *Acta Geotech.* **2022**, *17*, 5043–5057. [CrossRef]
73. Yang, J.; Wang, L.; Li, X.; Zhao, G. Research on micro-fracture mechanism of mudstone after wet-dry cycles. *Yanshilixue Yu Gongcheng Xuebao/Chin. J. Rock Mech. Eng.* **2014**, *33*, 3606–3612. [CrossRef]
74. Bull, A.J.; Fall, M. Curing temperature dependency of the release of arsenic from cemented paste backfill made with Portland cement. *J. Environ. Manag.* **2020**, *269*, 110772. [CrossRef]
75. Damidot, D.; Glasser, F. Thermodynamic investigation of the CaO Al_2O_3 $CaSO_4$ H_2O system at 50 °C and 85 °C. *Cem. Concr. Res.* **1992**, *22*, 1179–1191. [CrossRef]
76. Qian, J.; Yu, J.; Sun, H.; Ma, Y. Formation and Function of Ettringite in Cement Hydrates. *Kuei Suan Jen Hsueh Pao/J. Chin. Ceram. Soc.* **2017**, *45*, 1569–1581. [CrossRef]
77. Comboni, D.; Gatta, G.D.; Lotti, P.; Merlini, M.; Hanfland, M. Anisotropic compressional behavior of ettringite. *Cem. Concr. Res.* **2019**, *120*, 46–51. [CrossRef]
78. Bizzozero, J.; Gosselin, C.; Scrivener, K.L. Expansion mechanisms in calcium aluminate and sulfoaluminate systems with calcium sulfate. *Cem. Concr. Res.* **2014**, *56*, 190–202. [CrossRef]
79. Shi, Z.; Li, J.; Zhao, Y. Study on damage evolution and constitutive model of sandstone under the coupled effects of wetting-drying cycles and cyclic loading. *Eng. Fract. Mech.* **2021**, *253*, 107883. [CrossRef]
80. Song, X.; Hao, Y.; Wang, S.; Zhang, L.; Liu, W.; Li, J. Mechanical properties, crack evolution and damage characteristics of prefabricated fractured cemented paste backfill under uniaxial compression. *Constr. Build. Mater.* **2022**, *330*, 127251. [CrossRef]
81. Zhou, Y.; Yu, X.; Guo, Z.; Yan, Y.; Zhao, K.; Wang, J.; Zhu, S. On acoustic emission characteristics, initiation crack intensity, and damage evolution of cement-paste backfill under uniaxial compression. *Constr. Build. Mater.* **2021**, *269*, 121261. [CrossRef]